

Constraining mornings & evenings on distant worlds: a new semi-analytical approach and prospects with transmission spectroscopy

NÉSTOR ESPINOZA  ¹ AND KATHRYN JONES  ²

¹Space Telescope Science Institute, 3700 San Martin Drive, Baltimore, MD 21218, USA

²University of Bern, Center for Space and Habitability, Gesellschaftsstrasse 6, CH-3012, Bern, Switzerland

(Received; Revised)

Submitted to AJ

ABSTRACT

The technique of transmission spectroscopy — the variation of the planetary radius with wavelength due to opacity sources in the planet’s terminator region — has been to date one of the most successful in the characterization of exoplanet atmospheres, providing key insights into the composition and structure of these distant worlds. A common assumption made when using this technique, however, is that the variations are the same in the entire terminator region. In reality, the morning and evening terminators might have distinct temperature, pressure and thus compositional profiles due to the inherent 3-D nature of the planet which would, in turn, give rise to different spectra on each side of it. Constraining those might be fundamental for our understanding of not only the weather patterns in these distant worlds, but also of planetary formation signatures which might only be possible to extract once these features are well understood. Motivated by this physical picture, in this work we perform a detailed study on the observational prospects of detecting this effect. We present an open-source semi-analytical framework with which this information can be extracted directly from transit lightcurves, and perform a detailed study on the prospects of detecting the effect with current missions such as *TESS* and upcoming ones such as *JWST*. Our results show that these missions show great promise for the detection of this effect. Transmission spectroscopy studies with *JWST*, in particular, could provide spectra of each of the limbs allowing us to convey 3-D information previously accessible only via phase-curves.

Keywords: Exoplanet atmospheres; Exoplanets, Exoplanet astronomy

1. INTRODUCTION

The technique of transmission spectroscopy — the wavelength dependence of the planetary radius during transit (Seager & Sasselov 2000; Hubbard et al. 2001; Burrows et al. 2003; Fortney 2005), has been one of the most successful ones in the past decade to explore the composition and structure of exoplanet atmospheres, providing key insights into their interior structures and compositions (see, e.g., Kreidberg 2018, for a review). From an observational perspective, to obtain a transit spectrum researchers typically fit a transit model to precise wavelength-dependent lightcurves in order to

retrieve the transit depths, $(R_p/R_*)^2$, as a function of wavelength. Typically, the fitting procedure relies in one simple, but key assumption: the terminator region we observe during transit is homogeneous. There is already growing evidence that this assumption might actually be unrealistic in relatively hot ($T_{\text{eq}} > 1000$ K) exoplanet atmospheres, where the day-to-night differences might in turn imply different structures and overall compositions in their morning and evening¹ terminators (see, e.g., Fortney et al. 2010; Dobbs-Dixon et al. 2012; Kempton et al. 2017; Powell et al. 2019; MacDonald et al. 2020; Helling et al. 2020, and references therein). Constraining them might give precious insights into circulation

Corresponding author: Néstor Espinoza
 nespinoza@stsci.edu

¹ In this work, the morning and evening limbs are also referred to as the leading and trailing limbs, respectively.

patterns and compositional stratification which might probe to be fundamental for our understanding of the weather patterns in distant worlds. For example, hazes are expected to be photochemically produced and thus they would most likely be able to form in the dayside (Kempton et al. 2017; Powell et al. 2019). These could, in turn, be transported to the trailing limb, while clouds could be transported from the nightside (where they are expected to form due to the lower temperatures) into the leading limb, thus resulting in a drastically different transmission spectrum between them, and thus effective sizes of the radii of each limb (Kempton et al. 2017; Powell et al. 2019). Directly detecting this effect would not only serve to put theories like the ones proposed by Kempton et al. (2017) and Powell et al. (2019) to the test, but would directly impact on the fundamental assumptions of transmission spectroscopy studies to date, implying there is not *one* set of properties (e.g., abundances) to extract from transmission spectra. This is, in turn, critical to perform inferences on e.g., formation scenarios based on extracted molecular abundances with this technique (see, e.g., Öberg et al. 2011; Mordasini et al. 2016; Espinoza et al. 2017, and references therein).

Previous works (e.g., Dobbs-Dixon et al. 2012; Line & Parmentier 2016; Kempton et al. 2017; Powell et al. 2019; MacDonald et al. 2020) have already studied the prospects and impact of limb inhomogeneities on transit spectra. Overall, the consensus seems to be that there is already both observational and theoretical evidence that this is an effect that is important to consider and that might even be impacting current transit spectra. Line & Parmentier (2016), Kempton et al. (2017) and Powell et al. (2019) have already laid out the foundation of the theoretical aspects of detecting this effect, while MacDonald et al. (2020) has in fact studied publicly available transmission spectra in order to show that they can actually be explained as arising from two distinct temperature/pressure profiles. In this work, we explore these prospects from an observational perspective which aims at detecting the effect of limb asymmetries *directly in transit lightcurves*, such that interpretations can be made at a later stage on each of the limbs.

Detecting limb-asymmetries at the lightcurve level could have important impacts on how researchers typically approach transit spectroscopy for several reasons. First, it could imply that performing inference about the limbs on transit depths obtained through lightcurve fits using the classic Mandel & Agol (2002) symmetric transit model is subject to be biased, as the lightcurves would be essentially fit with the wrong model. If the limbs have different properties, their transit spectrum -and thus their “transit depths”- would be different, in-

jecting lightcurve asymmetries that these models cannot properly account for. Second, performing inference on the transit depths obtained through these symmetric transit models also necessitates a handful of assumptions in order to overcome the degeneracies that fitting a single transmission spectrum with two different temperature, pressure and abundance profiles imply. This, in turn, diminishes the discovery space to the assumptions made by our models, which might be quite a restrictive imposition, especially in the era of ultra-high spectrophotometric precision such as the ones the upcoming *James Webb Space Telescope (JWST)* will be opening up. Here, we propose instead that if indeed limb asymmetries can be detected in the transit lightcurves themselves, this would open up a whole new and direct framework for obtaining information about them. In this framework, we would be able to extract *two* “limb spectra” from a given transit lightcurve: one spectrum for each limb, which we could interpret individually at a later stage through, e.g., atmospheric retrievals and/or forward models. It is important to note that the essence of this proposition is not particularly new (it has already been suggested by the work of von Paris et al. 2016). Our contribution in this work is to perform a deep dive into (a) *how* we might actually perform this characterization in a fast and reliable way, (b) *what is the level of detectability* of this effect with current and near-future instrumentation and (c) to show how, in some cases, this might even be *the most efficient way of extracting this information* from transit lightcurves. Some of these points have already been touched upon by Powell et al. (2019) at different degrees of depth; here we expand and homogenize the discussion from an observational perspective, which we believe complements these previous works on this topic.

Our work is organized as follows. In Section 2 we present a new semi-analytical method to extract the transit depths from each of the limbs of an exoplanet. The core idea of this method was actually already put forward by von Paris et al. (2016), where each of the limbs of the exoplanet are modelled as stacked semi-circles. However, we expand on this modeling framework in that our calculation is made in a semi-analytical fashion, making use of geometrical arguments and the algorithm used by `batman` (Kreidberg 2015). This makes the lightcurve computation much faster than the numerical scheme described in von Paris et al. (2016), and allows us to expand it to account for sky-projected *planetary* spin-orbit misalignments. We present a python library to generate lightcurves with this new algorithm, `catwoman` (Jones & Espinoza 2020), in Section 2.1, provide an overview of the model and validate it against a

numerical implementation in Section 2.2. In Section 3 we present simulations in which we explore the feasibility of detecting this effect with current precise photometry such as that of the *Transiting Exoplanet Survey Satellite* mission (*TESS*; Ricker et al. 2014) and near-future instrumentation such as spectrophotometry to be obtained by the upcoming *JWST*. In Section 4 we present a discussion and implications of our results, along with a case-study on the exoplanet HAT-P-41b, which we use to demonstrate how extracting the spectrum of the limbs of this exoplanet might give insights into possible models that give rise to the observed transit spectrum by the *Hubble Space Telescope* (*HST*). We summarize our main conclusions in Section 5.

2. MODELING LIMB ASYMMETRIES IN TRANSIT LIGHTCURVES

The idea proposed by von Paris et al. (2016) to model the signatures of asymmetric limbs in transit lightcurves involves a very simple concept: approximate the terminator regions of the leading and trailing limbs as two stacked semi-circles with different radii. In essence, the idea is that each limb produces an independent transit spectrum that we ought to recover by modeling the lightcurve imprinted by them. In that work, the authors used a numerical framework to compute the resulting lightcurve, which is relatively computationally expensive. Here we use the same idea but tackle the problem from a different angle: instead of using a numerical approach, we employ a semi-analytical framework, which in turn allows for faster lightcurve computations. In this new framework, the stacked semi-circles are also allowed to be *rotated* with respect to the orbital motion, expanding thus the proposed framework by von Paris et al. (2016).

The basic problem we are trying to tackle is that of producing a transit lightcurve of two stacked semi-circles of (normalized, with respect to the stellar) radii $R_{p,1}$ and $R_{p,2}$ in front of their host star, where the semi-circles may be inclined with respect to the orbital motion by an angle φ . The geometrical configuration of the problem is depicted in Figure 1. We follow Kreidberg (2015) and assume a radially symmetric intensity profile $I(x)$, where $0 < x < 1$ is the normalized radial coordinate measured from the center of the star. With this, we can express the fraction of stellar light blocked by the object, δ , as (see Figure 1)

$$\delta = \sum_{i=1}^N I(x_m) \Delta A(x_m, R_{p,1}, R_{p,2}, \varphi, d), \quad (1)$$

where $x_m = (x_i + x_{i-1})/2$ is the middle point between x_i and x_{i-1} , and $\Delta A(x_m, R_{p,1}, R_{p,2}, \varphi, d)$ (for which we

shall refer to in what follows simply as ΔA) is the intersectional area between the stacked semi-circles and the iso-intensity band depicted in Figure 1, where $R_{p,1}$ and $R_{p,2}$ are the radii of the semi-circles, φ is the rotation of the base of the semi-circles with respect to the orbital motion of the planet and d is the distance between the center of the star and the semi-circles. Because the form of $I(x_m)$ is usually known/parametrized via so-called limb-darkening laws, the challenge of finding the lightcurve of this configuration of stacked, rotated semi-circles is to find ΔA . The full derivation of this is presented in Appendix A; we present an overview of our implementation and validation of our approach below.

2.1. Implementation and model overview

Our semi-analytic approach to the problem has been implemented in the `catwoman` library (Jones & Espinoza 2020), which is fully documented² and available on Github³. In practice, `catwoman`'s code-base is that of `batman` Kreidberg (2015), and as such the library inherits most of the high-level functionalities of this latter library. A `catwoman` lightcurve, thus, receives as inputs the time-of-transit center t_0 , the period P of the orbit, the scaled semi-major axis a/R_* , the inclination i of the orbit with respect of the plane of the sky, the eccentricity e and argument of periastron ω of the orbit, and a set of limb-darkening coefficients for any of the laws already available in `batman`. On top of these, `catwoman` takes as input the radii of each of the stacked semi-circles, $R_{p,1}$ and $R_{p,2}$, and the angle φ between the axis that connects them and the vector that follows the direction of motion in the orbit (see Figure 1).

The motivation behind allowing to define the angle φ in the lightcurve generation comes from the possibility of being able to detect the sky-projected spin-orbit misalignment of the *planet*, which is something the eclipse mapping technique for both lightcurves (Rauscher et al. 2007; Williams et al. 2006) and radial-velocities (Nikolov & Sainsbury-Martinez 2015) are able to do in principle. As will be shown in Section 3.3, detecting the effect of asymmetric lightcurves due to morning/evening terminator structural and/or compositional inhomogeneities almost guarantees the possibility of putting constraints on this angle, and ignorance on its value does not have a great impact on the detectability of the effect. One important point to consider on this parameter is that this defines the *instantaneous* angle between the axis that joins the semi-circles and the direction of the orbital motion (see Figure 1; orbital motion indicated with a

² <http://catwoman.readthedocs.io>

³ <https://github.com/KathrynJones1/catwoman>

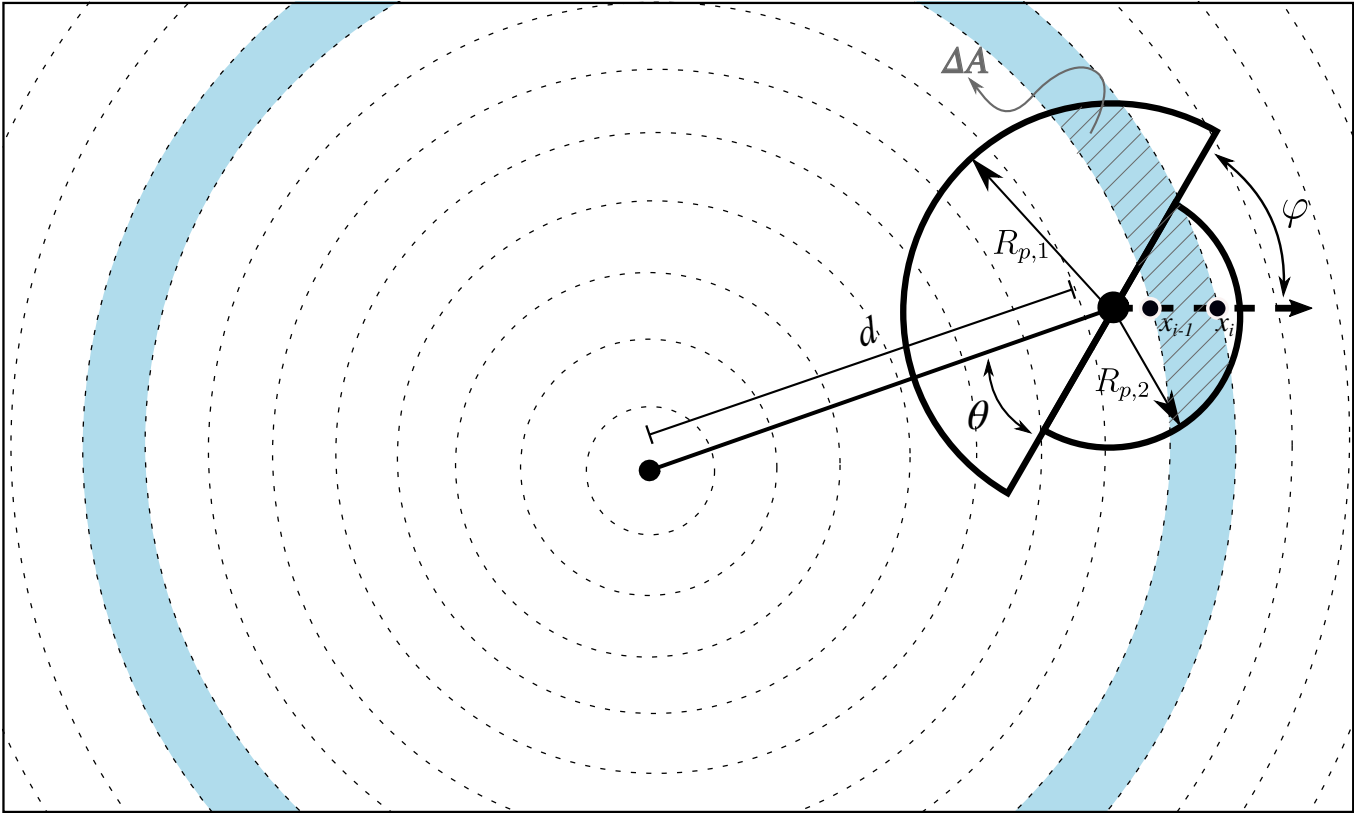


Figure 1. Diagram of the geometric configuration during transit of two stacked semi-circles (one of radius $R_{p,1}$; indicated by the arrow going up, and another of radius $R_{p,2}$; indicated by the arrow going down) that model the (possible) different limbs of an exoplanet transiting in front of a star. The area of the star has been divided into different sections of radius x_i (dashed circles) — between each subsequent section, the star is assumed to have a radially symmetric intensity profile (e.g., blue band between x_{i-1} and x_i above). In order to obtain the lightcurve such an object would produce, the challenge is to calculate the intersectional area between a given iso-intensity band and the stacked semi-circles, ΔA (blue band with dashed grey lines). Note the stacked semi-circles are inclined by an angle φ with respect to the planetary orbital motion (illustrated by the dashed arrow moving to the right), which accounts for the possibility of having planetary spin-orbit misalignments ($\varphi = \pi/2$ implies no spin-orbit misalignment). θ is the angle between the base of the semi-circles and the line that joins the centers, d .

dashed-line arrow). Because orbits as projected in the plane of the sky are curved in general, this means the axis that joins the semi-circles *rotates* when compared against a straight line projected in this plane. This effect has been implemented within `catwoman` as well (see Appendix A); we validate this implementation against a numerical implementation in the next sub-section.

2.2. Validation of the semi-analytical approach

In order to validate the semi-analytical approach presented here and implemented in the `catwoman` library, we built a numerical model that is also able to generate asymmetric lightcurves due to terminator inhomogeneities but through a completely independent and straightforward (albeit “brute-force”) approach. While by construction `catwoman` is able to reach any desired precision level (as that is a parameter that can be modified and is tested for convergence before running lightcurve model evaluations), our objective with

this alternative approach is to validate and illustrate that `catwoman` is indeed able to generate asymmetric lightcurves with accuracies of at least 10 ppm, which are the noise limits ultra-precise spectrophotometers like the upcoming *JWST* will be able to reach (Greene et al. 2016). Our implementation of this numerical scheme is also available in Github⁴, and is detailed below.

Our approach of this numerical version of the lightcurve generation of asymmetrical transits is very similar to that of von Paris et al. (2016), and consists of simply discretizing the plane of the sky into $n_p \times n_p$ “pixels” centered around the target star. Pixels within the star are filled with values between 0 and 1 according to a given intensity profile $I(\mu)/I(1)$, while positions that include either the planet or the sky are filled with zeroes. The precision on the lightcurves generated by this

⁴ https://github.com/nespinoza/numerical_catwoman

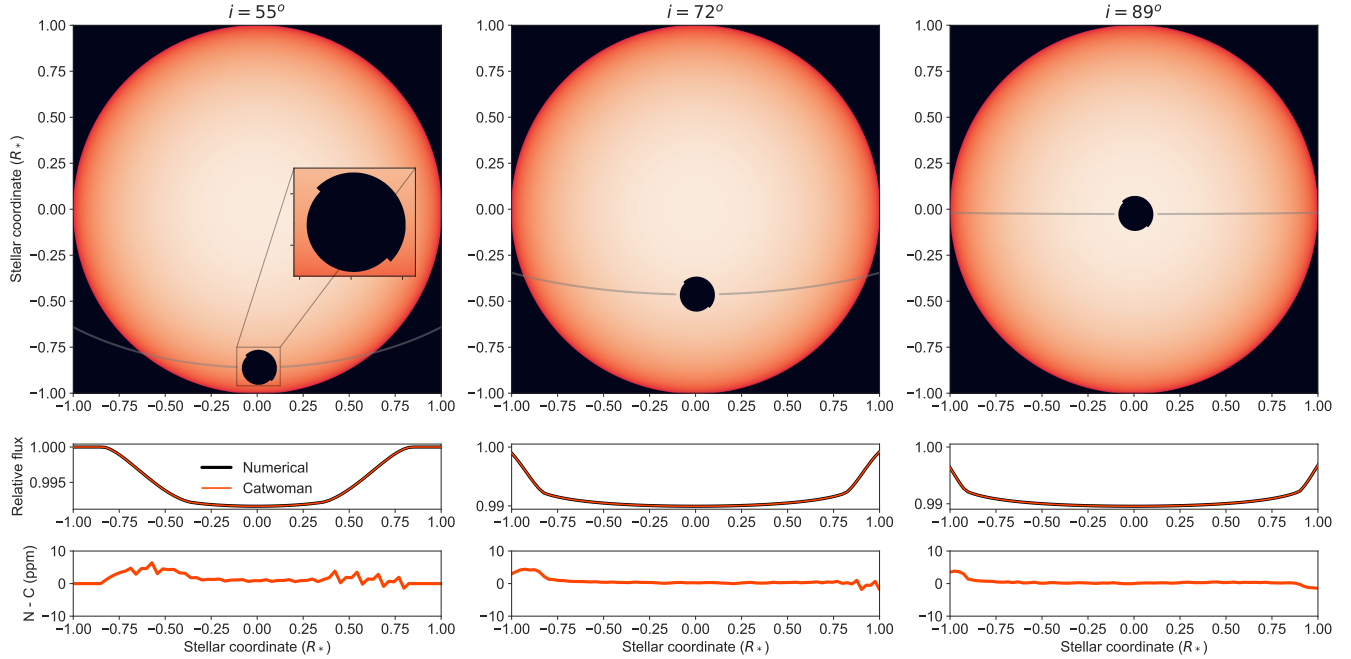


Figure 2. Comparison between a numerical implementation of the lightcurve generation of asymmetrical transits and the semi-analytical formalism presented in our work, implemented in the `catwoman` library. Examples are shown for orbital inclinations of 55° (left), 72° (middle) and 89° (right) — all of them assume a period of 3 days, a quadratic limb-darkening law ($u_1 = 0.3$, $u_2 = 0.2$), $a/R_* = 1.5$ and zero eccentricity. The top images are snapshots of our numerical model which include a limb-darkened star (orange) and a planet with asymmetric terminator regions ($R_{p,1} = 0.1$, $R_{p,2} = 0.09$ and $\varphi = -45^\circ$) transiting in front of it; middle panels show the retrieved lightcurves from both methods, and the bottom panels show the difference between the two. Most of the residuals observed in this latter panel are due to errors on our numerical model scheme (see text); by construction, our `catwoman` models in these computations had a 1 ppm error limit.

scheme, thus, can be optimized by simply increasing n_p . In practice, this is implemented by populating a matrix of dimensions (n_p, n_p) , on which we first fill all pixels within a distance of $n_p/2$ from the center of this matrix (i.e., $(n_p/2, n_p/2)$) with intensities given by the defined intensity profile (a quadratic law in the case of our implementation) — all other pixels are filled with zeroes. With this, we sum all the pixel values to compute our out-of-transit flux. Our algorithm then, using as inputs the coordinates of the center of the planet with respect to a reference frame centered on the star (X, Y) at each time-step and the input angle φ , computes the slope of the orbital motion $s = dY/dX$ by simple differences at each time-step i , i.e., $s_i = (Y_{i+1} - Y_i)/(X_{i+1} - X_i)$. This is then used to compute the instantaneous rotation of the axis that joins the stacked semi-circles with respect to the orthogonal system that defines the (X, Y) positions as $\arctan(s_i) + \varphi$. This axis is then used to separate the areas covered by both semi-circles, pixels inside of which are set to zero.

We use this simple numerical scheme to validate the semi-analytical framework developed in this work by computing a set of cases including a challenging one in which the planetary orbit is significantly curved. This

latter case allows us, in turn, to verify that our method outlined in Appendix A is correctly accounting for the rotation of the axis that joins the semi-circles with respect to the orthogonal system that defines the (X, Y) positions of the planet. To generate this, we simulate an exoplanet with a period of 3 days, time-of-transit center $t_0 = 0$, scaled semi-major axis $a/R_* = 1.5$ and zero eccentricity for three inclinations: $i = 55^\circ$, 72° and 89° degrees. For the star, we define a quadratic limb-darkening profile with $u_1 = 0.3$ and $u_2 = 0.2$. As for the physical properties of the planet, we assume it to have asymmetric terminator regions with $R_{p,1} = 0.1$, $R_{p,2} = 0.09$ and $\varphi = -45^\circ$. Planetary positions (X, Y) were obtained using `catwoman` (which uses the exact same method as `batman` to calculate them) for 100 equally spaced timestamps between -0.5 and 0.5 days. We performed numerical simulations with $n_p = 2500$, 5000 , 10000 , 20000 and 40000 (i.e., doubling the number of pixels on each side of our matrix), and found that the maximum flux changes roughly halved as well between each of those runs. These changes reached 4 ppm between $n_p = 20,000$ and $n_p = 40,000$, which we consider as our maximum error on the fluxes of our numerical scheme when selecting this latter number for n_p . Simulations using both

our numerical (with $n_p = 40,000$) and semi-analytical (through the `catwoman` library, with a maximum error set to 1 ppm⁵) schemes are presented in Figure 2. As can be observed, the differences between both are *very* small; they reach peak differences of less than 7 ppm — most of which are explained by the errors defined by our numerical scheme.

For all practical purposes, these limits give us confidence that our semi-analytical framework works as expected for precisions which are better than current and near-future instruments such as *JWST*, which is expected to reach about 10 ppm lightcurve precisions (Greene et al. 2016). We note that the speed increase of the `catwoman` library in comparison to the numerical implementation is huge: `catwoman` takes a couple hundreds of milliseconds to generate a lightcurve in a 2.9 GHz Intel Core i9 processor. The numerical implementation takes tens of seconds to generate the same model, although this latter one is a pure-Python code, whereas the `catwoman` library is a mixture of Python and C. In general, in experiments made with this processor, `catwoman` takes about twice the time `batman` takes to generate a lightcurve. This is consistent with the fact that the `catwoman` code-base is inherited from the `batman` one, and goes to show that the analytical part of `catwoman` is as fast as `batman`'s — only that we perform it twice, one for each of the stacked semi-circles.

3. DETECTABILITY OF THE EFFECT

Although the pioneering study of von Paris et al. (2016) already tried to detect the effect of asymmetric transit lightcurves produced by non-uniform cloud cover on precise data of three exoplanets obtained by the *Kepler* mission and *HST*, a systematic study of the detectability of the effect has not been done either on real or simulated transit lightcurves. Such a study is very timely as the *TESS* satellite (Ricker et al. 2014) has just started its extended mission re-observing some of the most promising targets to detect this effect and as *JWST* prepares for launch. These missions have a key advantage over *Kepler*: they allow us to target objects with large scale-heights, for which this effect should be more prominent in the data even if they are observed over shorter time-scales.

The question of the detectability of the effect in a given dataset is, however, a complex one. It is not only related to the precision of the lightcurves themselves in order to be able to detect the effect (which is evident

will depend on the difference between the effective size of the terminator region on the leading and trailing limb of the exoplanet), but also to the correlation between the parameters that could impact on a transit lightcurve. It could be that the lightcurve indeed is asymmetric but a given transit parameter is able to correct for this if a symmetric model is used. Indeed, von Paris et al. (2016) identified that the evidence for asymmetric lightcurves is heavily impacted by the knowledge of the ephemerides: a small shift in the time-of-transit center on a symmetric transit model could lead to an equally good fit to one with an asymmetric model, even for intrinsically asymmetric lightcurves. As such, in order to *claim* the detection of this effect, one needs to perform proper model comparison. In this work, we choose to use bayesian model evidences to this end. In particular, we assume both the symmetric and asymmetric lightcurve models are equiprobable a-priori, which implies the difference between the log-evidence of an asymmetric lightcurve, $\ln Z_A$ to the one obtained from a symmetric one, $\ln Z_S$, $\Delta \ln Z = \ln Z_A - \ln Z_S$, is equal to

$$\Delta \ln Z = \ln \frac{Z_A}{Z_S} = \ln \frac{\mathcal{P}(A|\text{Data})}{\mathcal{P}(S|\text{Data})},$$

where $\mathcal{P}(A|\text{Data})$ is the probability of the asymmetric model given the data and $\mathcal{P}(S|\text{Data})$ is the probability of the symmetric model given the data.

In what follows, we simulate asymmetric lightcurves using the `catwoman` library with *JWST*-like and *TESS*-like cadences, in order to study how the detectability of the effect changes with our knowledge of different parameters of the model and the lightcurve precision using bayesian evidences as the metric for detectability. We decide not to generate simulations for *HST*, as the gaps between orbits of the observatory imply a special, case-by-case analysis on the detectability of the effect — we leave such a study for future work. For each of the cases described below we generate asymmetric lightcurves with a range of radius differences between the leading (“morning”) and trailing (“evening”) limbs. We parametrize this in our simulations in terms of the corresponding “transit depth” each side of the planet implies. To this end, we fix $R_{p,1}/R_*$ to 0.1 in order to emulate a typical hot Jupiter planet-to-star radius ratio, and then define

$$R_{p,2}/R_* = \sqrt{(R_{p,1}/R_*)^2 + 2\Delta\delta}, \quad (2)$$

where $\Delta\delta$ is the morning-to-evening transit depth difference. The factor of 2 in front of this term stems from the fact that here we define $\Delta\delta$ as the transit depth difference *between the transit depth imprinted in the lightcurve by each of the stacked semi-circles*. In

⁵ In `catwoman`, we inherit the maximum allowable truncation error for numerical integration from `batman`; see Section 3.4 in Kreidberg (2015).

other words, $\Delta\delta = \delta_2 - \delta_1$, where $\delta_i = (1/2)(R_{p,i}^2/R_*^2)$. While there is no consensus in the literature as to how small or large morning-to-evening transit depth differences should be (e.g., Kempton et al. (2017) predict between 100-400 ppm differences for WASP-121b; Powell et al. (2019) predict values as large as 1000 ppm) we choose here to take a conservative upper limit on the effect of 500 ppm; in our simulations, thus, $\Delta\delta$ ranges from 5 to 500 ppm in 30 log-spaced bins. For each of those combinations, we simulate 5 datasets of noisy transit lightcurves with noise levels σ_w ranging from 10 to 1000 ppm in 30 log-spaced bins as well. We calculate the average of the log-evidences for symmetric and asymmetric models fitted to that data in each $(\Delta\delta, \sigma_w)$ pair, which is then used to compute the difference between the log-evidences. In all of our simulations the period is set to 1 day, the semi-major axis to stellar radius ratio to $a/R_* = 10$, inclination to 90 degrees, and a circular orbit is assumed. We note this set of parameters define a worst-case scenario for the detection of the effect. The reason is that most of the information used to infer the limb asymmetries comes from ingress and egress, as has already been shown by previous works (see, e.g., von Paris et al. 2016; Kempton et al. 2017; Powell et al. 2019). The ingress/egress duration in a circular orbit is given by

$$\tau = \left(\frac{P}{\pi}\right) \left(\frac{1}{\sqrt{1-b^2}}\right) \left(\frac{R_p}{R_*}\right) \left(\frac{R_*}{a}\right).$$

In the case of these simulations, this gives an ingress/egress duration of only $\tau = 4.6$ minutes. As a comparison, the archetypal hot Jupiter HD 209458b (Charbonneau et al. 2000; Henry et al. 2000) has $\tau = 25.7$ minutes. Our simulations in this Section, thus, can be seen as *lower limits and/or very conservative estimates* on the detectability of the effect. We explore the variation of the precision on the limb asymmetries with ingress/egress duration along with a case-study of a real hot Jupiter in Section 4.

To perform the fits to our simulated data, we implemented `catwoman` (Jones & Espinoza 2020) in the `juliet` (Espinoza et al. 2019) package, which already implements `batman` (Kreidberg 2015) for symmetric lightcurve models, and allows us to compute bayesian evidences for our model comparison using MultiNest (Feroz et al. 2009) via the PyMultiNest wrapper (Buchner et al. 2014). Table 1 lists the prior distributions used in our experiments — we explain and detail each of those below.

3.1. Detecting asymmetric lightcurves with JWST

In order to perform the simulations for *JWST*-like observations, we needed to calculate a typical cadence for

observations to be taken by the observatory for time-series exposures. In this work, we focus on observations aiming to constrain the effect using NIRISS/SOSS, as this instrument allows us to obtain spectra all the way down to $0.6 \mu\text{m}$ through the combination of data from Order 1 ($1 - 3 \mu\text{m}$) and 2 ($0.6 - 1 \mu\text{m}$). Given that the largest limb asymmetries seem to be in the transition between optical and NIR wavelengths (see, e.g., Kempton et al. 2017; Powell et al. 2019), we believe this will usually be the instrument of choice to characterize the effect for bright targets (with the alternative being, of course, NIRSpec/PRISM for fainter targets). Considering the reset time for this instrument is relatively short (couple of seconds), it sufficed for our work to know the typical integration time of a *JWST* observation with SOSS. For a solar-type, $V = 11$ star, according to the *JWST* Exposure Time Calculator⁶ (ETC; Pontoppidan et al. 2019), the typical integration time is 100 seconds, which is consistent with the values used in the `catwoman` and `batman` fits.

Table 1. Priors and parameters used for our experiments in Section 3 for the `catwoman` model fits. The `batman` fits used similar priors, with the caveat that this model assigns a uniform radius for the entire planet R_p/R_* for which we use the same prior as for $R_{p,1}/R_*$ below, and doesn't fit for φ . $U(a, b)$ below stands for a uniform distribution between a and b .

Parameter	Prior	Comment
P (days)	—	Fixed to 1
T_0 (days)	$U(-0.1, 0.1)$	Fixed to 0 when assumed known.
$R_{p,1}/R_*$	$U(0, 1)$	
$R_{p,2}/R_*$	$U(0, 1)$	
φ (deg)	$U(-90, 90)$	Only used in Section 3.3. Fixed to 90 otherwise.
q_1 ^a	$U(0, 1)$	Fixed to 0.25 when assumed known.
q_2 ^a	$U(0, 1)$	Fixed to 0.3 when assumed known.
e	—	Fixed to 0
ω	—	Fixed to 90
a/R_*	—	Fixed to 10
b	—	Fixed to 0

^aThese parameters correspond to the parametrization presented in Kipping (2013) for sampling physically plausible combinations of the quadratic limb-darkening coefficients.

⁶ <https://jwst.etc.stsci.edu/>

dan et al. 2016), “saturation” is attained at about 20-60 groups per integration for NIRISS/SOSS, which implies maximum integration times between 40-80 seconds per datapoint in the time-series. We arbitrarily decided to use 20 seconds for the cadence of our simulations in order to simulate observations trying to target half-saturation values, which has been a typical strategy for *HST* observations⁷.

In this case we tried three different simulations, in order to illustrate the impact of different assumptions in this one-transit, 20-second cadence case: (a) one in which everything but the radii of both sides of the exoplanet $R_{p,1}$ and $R_{p,2}$ are known, (b) one in which everything but the radii and the limb-darkening coefficients of the star are known, and finally (c) one in which everything but the radii, the limb-darkening coefficients of the star and the time-of-transit center are known. The limb-darkening law that was assumed to generate and fit the lightcurves was a quadratic law with $(u_1, u_2) = (0.3, 0.2)$, which are representative values for solar-type stars. In our `juliet` fits, we assumed the uninformative priors for two-parameter limb-darkening laws proposed by (Kipping 2013) for the cases in which limb-darkening was assumed to be unknown; for the time-of-transit center, a uniform prior with a width of 4.8 hours around the real predicted time of transit center was imposed. The results for these simulations are presented in Figure 3.

As can be observed from the simulations, the asymmetric transit lightcurves should be detectable (i.e., $\Delta \ln Z \gtrsim 2$) for morning-to-evening depth differences above around 25 ppm for a wide range of precisions at least in white-light (i.e., adding all the flux over the entire wavelength range of a given instrument), where *JWST* observations should achieve tens of ppm precisions per point in the transit lightcurves, and as long as the ephemerides are well known and constrained. If they are not, however, as can be observed in the rightmost panel of Figure 3a, the actual detection of the effect becomes extremely challenging because, as it has been already noted by von Paris et al. (2016), changes in the time-of-transit center in a symmetric model can account for the asymmetry in the lightcurve. The changes in this timing are very small — only a couple of seconds of shifts in the time-of-transit center suffice to mimic the asymmetry in the transit lightcurves (see Section 4.3 for details). This implies that to detect this effect in white-

light, very precise timings are needed in order to claim a detection.

It is important to note that although from the above results the detection of the effect *directly* in the white-light lightcurves even with *JWST*-like precisions seems relatively challenging to do with only one transit in the absence of precise timing constraints, the observatory has the advantage that it can perform spectrophotometry and, thus, the effect can be detected through the wavelength dependence of the radii at each side of the terminator region, as has already been highlighted by Powell et al. (2019) — see also Section 4. In particular, NIRISS/SOSS can produce extremely precise (tens of ppm) white-light transit lightcurves in Orders 1 and 2, which can be used to claim a detection of the effect using these white-light transit lightcurves alone at much higher significance levels (and thus be sensitive to much lower morning-to-evening depth differences) than the ones shown here. Lightcurves like these, in addition, should provide very precise morning and evening depths. Figure 3b and 3c show an example lightcurve fit on a 50 ppm-precision lightcurve, where the injected morning-to-evening depth difference was of 270 ppm. As can be seen in Figure 3b, both evening and morning depths are highly correlated, but nonetheless provide precise constraints in this case on each of about 16 ppm, giving in this case a retrieved morning-to-evening depth difference of $\Delta\delta = 257 \pm 32$ ppm — fully consistent with the input value⁸. Most of the information to constrain those depths come from ingress and egress, as is evident in the residuals (blue for `catwoman`, red for `batman`) of Figure 3c. We provide a deeper understanding on the relation between lightcurve precision and morning and evening depth precisions in Section 4.

3.2. Detecting asymmetric lightcurves with *TESS*

Although the *TESS* mission has a significantly smaller aperture than *JWST*, the cadence and types of observations the mission does are excellent for the detection of asymmetries in transit lightcurves. The mission not only attains an exquisite precision, but it is also able to observe several transits of the same exoplanet, mitigating the problem we observed with only one transit in *JWST*-like observations like the ones simulated in the previous subsection. We performed the same simulations that we did for *JWST* but with a *TESS*-like cadence of 2-minutes, where we only consider observations on a 27-day period (i.e., one *TESS* sector). Inter-

⁷ But see <https://jwst-docs.stsci.edu/methods-and-roadmaps/jwst-time-series-observations/tso-saturation>.

⁸ Note the precisions of each limb do not add in quadrature to the constraint on the limb-difference. This is expected, again, due to the correlation between each of the limb depths.

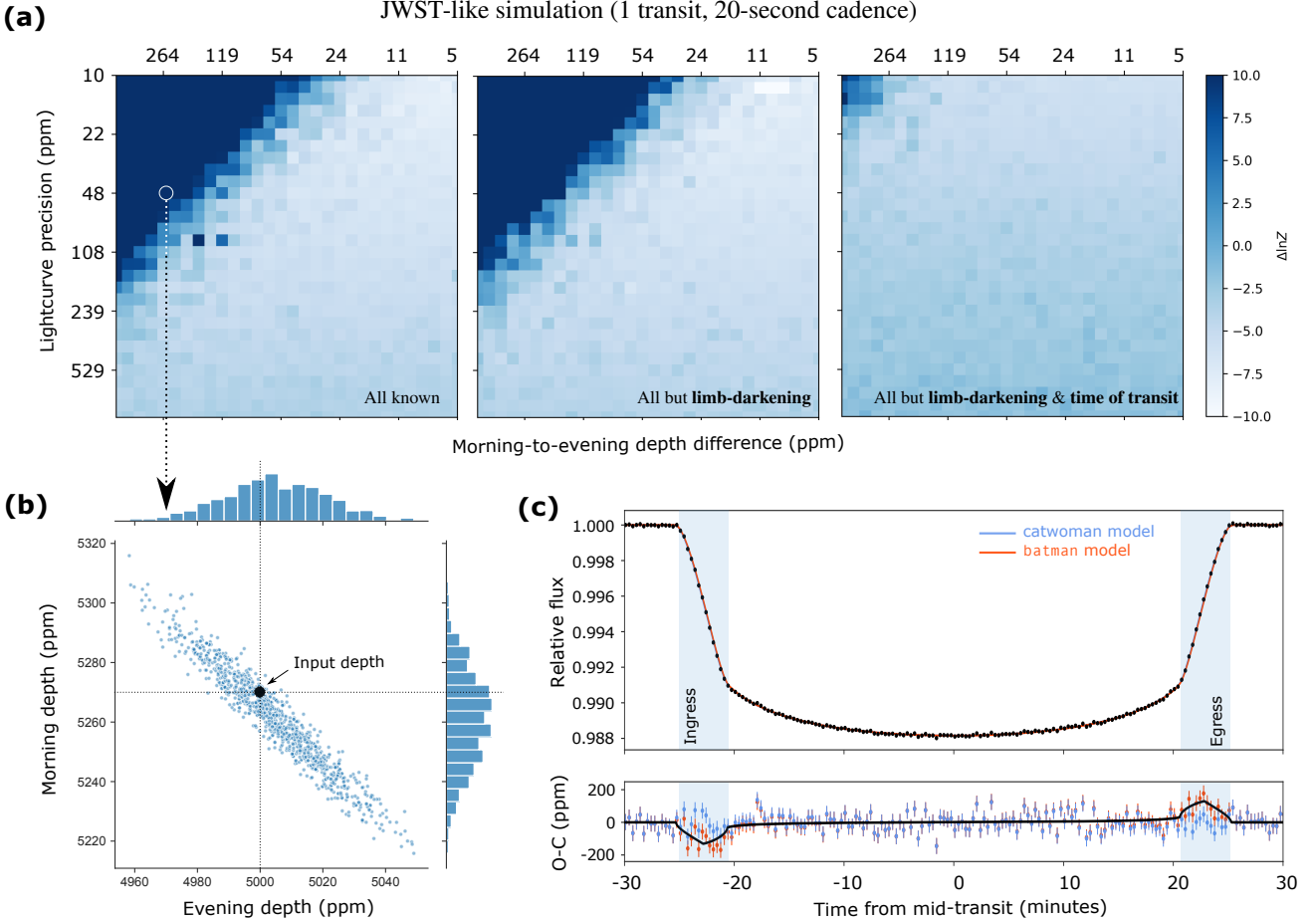


Figure 3. Injection and recovery simulations of asymmetric lightcurves due to differences in the morning and evening terminator for *JWST*-like cadence (1 transit, 20-second cadence, 1-day period, 4.6-minute ingress/egress duration). (a) Detection map in the morning-to-evening depth difference versus lightcurve precision (both in ppm) map; darker regions show the detectability region of the effect when all the parameters other than the planetary radius is known (left), other than the planetary radius and limb-darkening (center) and other than the planetary radius, limb-darkening and time-of-transit center (right). Colors indicate the difference between the log evidences, $\Delta \ln Z$, of asymmetric (**catwoman**) models and symmetric (**batman**) models. Note how if the time-of-transit center is unknown, detecting the effect gets very challenging. (b) Posterior samples of the morning and evening limb depths on an example lightcurve with 50 ppm precision and a morning-to-evening depth difference of 270 ppm; note the high correlation (but good recovery) of the limb depths; true input value is marked with dashed lines. (c) Simulated transit lightcurve corresponding to the posterior shown in (b); models (**batman** in red; **catwoman** in blue) are indistinguishable in the top panel; the residual panel, however, clearly shows the differences: the residuals using the **batman** model (red) show bumps at ingress and egress; the **catwoman** model residuals (blue) correctly model those bumps. The black line in the bottom panel shows the difference between the best-fit **batman** and **catwoman** models.

estingly, the three cases that we tried in the previous sub-section (all known, all but limb-darkening known and all but limb-darkening and the time-of-transit center known) all resulted in practically identical results — we show the one corresponding to the case in which all the parameters are assumed to be known but the radius, the limb-darkening coefficients and the time-of-transit center in Figure 4.

As can be observed, the results are very similar to the ones of *JWST*. This is a combination of the fact that there is about a 27-fold increase in the number of trans-

sits, which helps with the 6-fold increase on the cadence of the observations as compared to the *JWST* ones. The fact that there are more transits, in addition, helps with the problem *JWST* will face related to the ephemerides where in our analysis, of course, there is an implicit assumption regarding no possible deviations from strict periodicity in the transit times. We reiterate, however, that our simple simulations in Section 3.1 did not consider the huge advantage that *JWST* has over *TESS* regarding the ability to measure wavelength-dependent transits, which should in turn break the degeneracy with

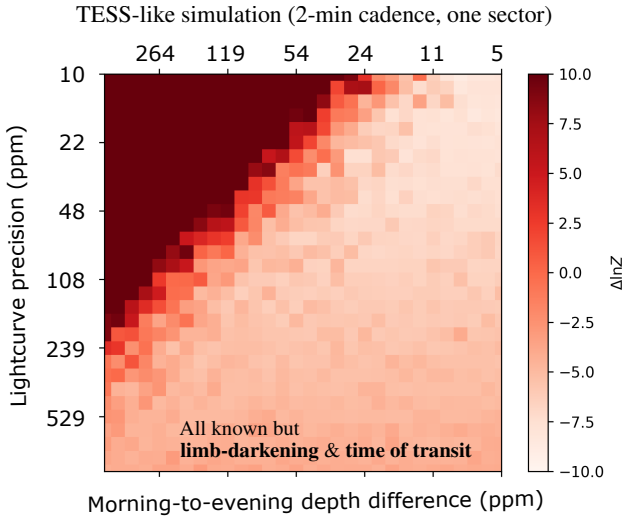


Figure 4. Simulations of asymmetric lightcurves due to differences in the morning and evening terminator transmission spectra for *TESS*-like cadence (2-minute cadence, one sector, 1-day period, 4.6-minute ingress/egress duration) when all the parameters other than the planetary radius, limb-darkening and time-of-transit center are known. Colors indicate the difference between the log evidences of asymmetric models and symmetric models (positive meaning odds ratios in favor of asymmetric lightcurve models).

the ephemerides as already suggested by Powell et al. (2019). We delve deeper into the benefits of wavelength-dependent *JWST* transit observations for detecting the limbs of exoplanets in Section 4.

Although few targets attain the precisions at which one might statistically distinguish between an asymmetric and a symmetric model directly from the transit lightcurves with *TESS* in one sector, the fact that many targets are observed by more than one sector makes this effect within reach of what *TESS* is currently able to detect. Targets in the *JWST* Continuous Viewing Zone (CVZ) are particularly appealing to try to detect this effect. For example, WASP-62b ($V = 10.3$), for which the median per point precision was 880 ppm during the prime mission in 2-minute cadence, has been observed to date in more than 20 sectors, providing a combined per-point precision per transit of about at least $880/\sqrt{20} \approx 200$ ppm — a promising precision level to constrain the effect of asymmetric limbs if we assume a simulation like the one in Figure 4 also applies to an exoplanet like WASP-62b.

3.3. Detectability assuming φ is not known

As a final test on the detectability of the effect, we explore whether our ignorance on the angle φ can im-

pact it; we take our *JWST*-like simulation as a proxy for studying this, given the similarity in the shape of the detectability maps presented between *JWST* and *TESS* in Figures 3 and 4. To explore this, we use a transit lightcurve whose parameters are defined by the same ones as in the previous experiments, but in this case we set $\varphi = 45$ degrees as the ground-truth, and set a uniform prior between -90 and 90 degrees for the parameter in our fits. Our results for a *JWST*-like simulation (using the same cadence as in Section 3.1) are shown in Figure 5 where in addition to the detectability map, we also show a portion of the posterior distribution of a simulation with the same properties as the one shown in Figure 3 for the case in which φ was fixed — i.e., a lightcurve precision of 50 ppm, and a morning-to-evening depth difference of 270 ppm.

As can be seen, the detectability region (i.e., the medium blue and dark-blue region) of the plot has shifted by a small amount with respect to the one presented in Figure 3 implying that a slightly better lightcurve precision is needed in order to detect the effect if the angle φ is not known a-priori. In addition, given our large prior on φ , we actually detect two posterior modes (of which we show only one in Figure 5): one allowing for positive and one allowing for negative values of φ , each swapping the posterior distributions between the evening and morning limb. This was expected by construction: a model with φ and a given value of $R_{p,1} = a$ and $R_{p,2} = b$ is the same as a model with $-\varphi$ with $R_{p,1} = b$ and $R_{p,2} = a$. If we take the mode with positive values for φ , we note that in this case the evening and morning depths themselves are much more uncertain. This gives rise to a retrieved morning-to-evening depth difference of 250^{+374}_{-113} ppm — again consistent, but much less precise than the constraint assuming a known value of φ presented in Section 3.1. The constraint on φ itself is also not very precise; for this particular simulation, we obtain $\varphi = 32^{+33}_{-20}$ degrees; fully consistent with the input value, but not very constraining to understand the underlying, true projected planetary spin-angle.

Before moving into the next Section, it is important to reiterate that the precisions and detectability limits shown here were obtained for a very conservative —worst-case scenario— system with a very small ingress/egress duration. As will be shown in Section 4.1, the odds of detecting the effect on systems which have better prospects for it (i.e., systems with longer ingress/egress durations) are in reality much higher. The lower limits we set here, thus, seem promising for the detection of the effect with current and near-future instrumentation.

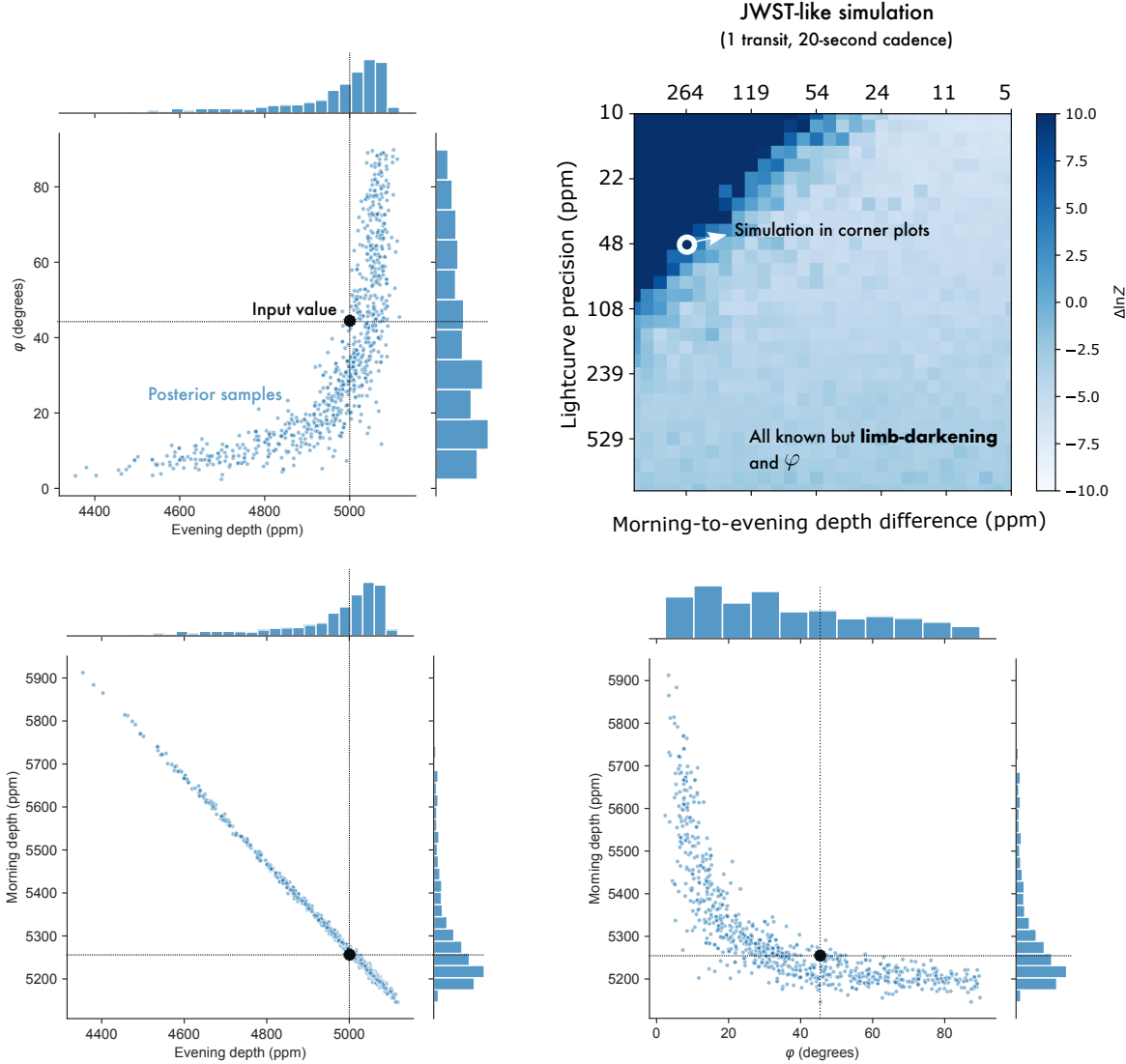


Figure 5. Simulations allowing for an unknown projected planetary spin angle, φ . The simulations presented above are similar to those shown on the center panel of Figure 3a, but this time also allowing for φ to be a free parameter. In addition to the detectability map, shown in the top right corner, we present a portion of the posterior distribution (which has two modes, allowing for both positive and negative values of φ ; see text) of the limb depths and angle φ as corner plots for the very same limb difference (270 ppm) and lightcurve precision (50 ppm) as that shown in Figure 3 (indicated here as a white circle in the top right detectability plot. Black dot on the corner plots indicates the true input value.)

4. DISCUSSION

In previous sections, we have presented both the details of our semi-analytic framework for generating asymmetric transit lightcurves due to morning/evening terminator heterogeneities — including its validation against simpler (but more computationally expensive) models — and a study of the detectability of the effect with current missions like *TESS* and future observatories like *JWST*. Although our results are encouraging for the detection of the effect, there are many aspects to pay attention to when performing lightcurve analyses

and/or when planning observations to detect the effect, including complementary methodologies, which we discuss below.

4.1. Asymmetric terminator depths precision

While in Section 3 we presented lower limits on the statistical detection of the effect on transit lightcurves based on bayesian evidences, an important aspect of interpreting transit lightcurve fits with the semi-analytic model presented in this work will involve constraining the actual measured transit depths of each side of the

planet. This will be useful not only to extract transit spectra of the different limbs when using wavelength-dependent lightcurves such as the ones to be obtained by *JWST*, but also to compute the maximum possible transit depth differences allowed by the data when analyzing broadband data such as the one from missions like *TESS*.

An important detail to consider when extracting transit depths from asymmetric limbs is the fact that the observable quantities that are directly constrained by the data are the areas of each of the semi-circles through the transit depths each of them produce. In symmetric models, where the limbs are assumed to be equal, the transit depth is simply $\delta = (R_p^2/R_*^2)$ — the projected area of the planet over the projected area of the star. In the asymmetric case, however, the projected area of the *semi-circles* are the quantities of interest, — the transit depth of each limb being given by $\delta_i = (1/2)(R_{p,i}^2/R_*^2)$. This is what effectively defines the transit spectrum of each limb and is, in turn, what should be used to compare against theoretical transmission spectroscopy models.

Figure 6 shows how the precision of the transit depths of each limb depend on the lightcurve precision, as well as the precision of the entire area of the planet, defined by the depth $\delta_1 + \delta_2$, for the case of the exoplanet simulated in Section 3 with an ingress/egress duration of $\tau = 4.6$ minutes (solid lines). As can be seen, the precision on the transit depth of the entire planet is always much smaller than the corresponding for both semi-circles, but the relationship between the two is not simple, as the transit depths of the semi-circles are highly correlated with each other. Indeed, the transit depth of the entire planet is constrained by the *entire lightcurve*, whereas the transit depths of each side of the planet (sampled by the semi-circles in our model) are mostly constrained by ingress and egress. This implies, in turn, that this latter precision would of course increase on systems with larger ingress/egress durations, which in many cases might be the optimal ones to target in order to maximize the chances to unveil this effect.

The simulations presented in Section 3 for $\tau = 4.6$ min. ingress/egress durations were performed to show lower-limits on the detection of the effect, and even in those cases the odds were very favorable given current (e.g., *TESS*) and future (e.g. *JWST*) lightcurve precisions and cadences. Hot Jupiters typically have longer ingress/egress durations, and some of the already characterized ones by missions like, e.g., *HST*, show good prospects for the detection of the effect as well. As an example, we repeat the *JWST* simulations in Section 3 for HAT-P-41b, which we select as is one of the most

thoroughly characterized ultra-hot Jupiters in transmission — all the way from near-UV, optical and up to near-infrared wavelengths (Wakeford et al. 2020; Lewis et al. 2020; Sheppard et al. 2021). We tune the physical and orbital parameters of the system to the ones used in Wakeford et al. (2020), which imply a 23.9 minutes ingress/egress duration. The cadence (53 seconds) and number of datapoints (500) for our simulations are set to the ones optimized by PandExo⁹ (Batalha et al. 2017) using NIRISS/SOSS as the instrument of choice such that SUBSTRIP256 does not saturate (which would be the setup of choice in order to obtain simultaneous spectroscopy in the near-infrared and the optical through Orders 1 and 2 for this target¹⁰). For consistency, we set the limb-darkening coefficients to the average ones on Order 1 of NIRISS/SOSS (but we note these do not impact on the overall precision and detectability, as was already shown in Section 3). The resulting precisions of this experiment are presented in Figure 6 as dashed lines. As can be observed, the precision change on the transit depths of each of the limbs is significant, and ranges from a 60% to 70% improvement in it. The precision change in the transit depth of the entire planet, however, is much smaller (and driven mainly by the difference in the absolute transit depths and transit durations), which acts as a baseline in showing quantitatively how the prospects of detecting asymmetric limb-differences are very sensitive to the ingress/egress duration.

One might argue that in Figure 6, one could observe two transits of the exoplanet with 4.6 min. ingress/egress duration in order to match the signal-to-noise of the exoplanet with the 23.9 min. ingress/egress duration. Although this would be true if the observatory only targeted the transit event, in practice there are observational overheads (like, e.g., pre-post transit baselines, and overall observatory overheads beyond clock time on-target) that have to be included in that reasoning. For instance, the time recommended in the *JWST* documentation¹¹ one should spend in a target during a transit is given by the dwell equation, which reads

$$T_{\text{dwell}} = 0.75 + \text{MAX}(2, T_{14}) + T_{14} + 1 \text{ hr}, \quad (3)$$

where T_{14} is the transit duration in hours. The exoplanet with an 4.6 min ingress/egress duration has a 1-hour total transit duration, which gives $T_{\text{dwell}} = 4.75$.

⁹ <https://exoctk.stsci.edu/pandexo>

¹⁰ We note HAT-P-41b saturates below about 2 microns with NIR-Spec/PRISM, which is the reason why we don't discuss this instrument in the context of this exoplanet.

¹¹ <https://jwst-docs.stsci.edu>

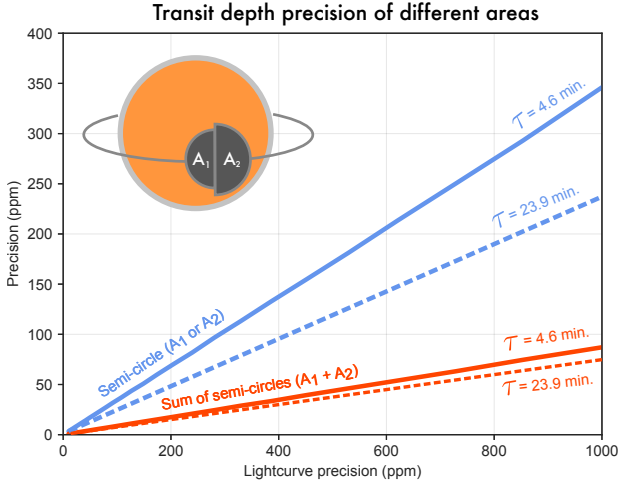


Figure 6. Transit depth precision on the semi-circles (transit depth defined as $\delta_i = (1/2)(R_{p,i}/R_*)^2$, with $R_{p,i}$ being the area of semi-circle i ; blue lines) and their sum (whose transit depth is $\delta_1 + \delta_2$; red lines) as a function of lightcurve precision. Precisions for systems with short (4.6 min., solid lines) and long (23.9 min., typical for hot Jupiters) transit ingress/egress durations, τ , are presented. **Main point:** Transit depth precisions of the limb of exoplanets are much less precise and much more dependant on transit ingress/egress duration than the transit depth produced by the entire area of the planet (i.e., the classically defined “transit depth”).

The exoplanet with a 23.9 min ingress/egress duration has a 3.6-hour transit duration, $T_{\text{dwell}} = 8.95$. Two transits of the 1-hour transit duration target would imply a requested time of 9.5 hours, which is at least half an hour more expensive than the 3.6-hour transit duration target — all this without considering extra observatory overheads. The conclusion, thus, is that the efficiency of the time and targets to be requested to detect the effect have to be studied on a case-by-case basis.

In addition to the above, it is also important to note that the posterior distributions of the limbs show typically non-negligible correlations (see, e.g., Figures 3 and 5). This is important to consider because this covariance carries extra information that could become important when performing inference on the limbs (through, e.g., atmospheric retrievals). In our experiments, we observed the shape of the posterior distribution (measured through the correlation — i.e., the covariance divided by the standard deviations of the marginal posterior distribution of each limb) remained fairly constant across the parameter space covered in our work; it simply shrinks as better precisions are achieved. We also found the posterior distribution of the limbs is very well approximated in the case of a known angle ϕ by a two-dimensional

gaussian distribution, which is characterized not only by the mean and standard deviation of the marginal posterior distributions, but also by the covariance between the limbs. We provide a practical example of how to use this information in a retrieval framework in the next sub-section.

4.2. The importance of constraining limb spectra

In order to showcase the importance of directly using transit lightcurves to constrain the limbs of exoplanets, and demonstrate that this indeed might be *the most efficient avenue to constrain the transit spectrum of the limbs*, we use HAT-P-41b as a case-study, using both real *HST* data and simulated *JWST* observations.

We first analyze the data presented in Wakeford et al. (2020), Lewis et al. (2020) and Sheppard et al. (2021) using the retrieval framework developed in MacDonald et al. (2020), namely, one in which the *transmission spectrum* is fit with a model using *two* different atmospheric structures, each of which represents one of the limbs. To this end, we use and slightly modify the “chemically consistent” CHIMERA¹² atmospheric retrieval framework of Line et al. (2013), such that two transmission spectra are modeled at each iteration of the algorithm. Each of those has a different temperature and cloud structure, as well as different C/O ratios; the temperature at the top of the atmosphere is forced to be always colder for one limb than for the other in order to simulate energy redistribution processes that might be happening between the limbs. Once those are computed, each model transit depth is multiplied by 1/2 in order to compute the spectra of each of the limbs, δ_i . These are then added together to form the “combined” transit depth that we compare against the *HST* transit spectrum. We decide to leave the metallicity, the 10 bar radius, and the overall temperature-pressure profile shape (other than the temperature at the top of the atmosphere) as common parameters between the limbs, as we assume the *HST* data would not be sensitive to those parameters. The retrieval is performed using nested sampling with the the pymultinest library (Buchner et al. 2014) which makes use of the MultiNest (Feroz et al. 2009) algorithm. The full set of priors used for our CHIMERA atmospheric retrievals in what follows are presented in Table 2.

The best-fit retrieval to the *HST* data using this two-limb retrieval framework is presented on the top panel of Figure 7. Posterior credibility intervals for each parameter fit in the retrieval are presented in the second column of Table 3. As can be seen in Figure 7, while the

¹² <https://github.com/mrline/chimera>

retrieved transit spectrum follows the data fairly well, the individual retrieved limb spectra shows a wide range of possible solutions, suggesting that they are fairly unconstrained by the data. Indeed, the overall posterior values for all parameters are largely indistinguishable between the limbs. For example, the temperatures at the top of the atmosphere are 1210^{+227}_{-132} K and 1522^{+519}_{-241} K for the “cold” and “hot” limbs, respectively, which are completely consistent with each other. The rest of the parameters, while fairly unconstrained by the data, all point towards a cloudy nature in HAT-P-41b’s atmosphere; our solution suggest a relatively high-altitude cloud-deck, whose base is at about 10 mbar — a picture in very good agreement with the retrieval analyses performed in Lewis et al. (2020).

The next experiment we ran consisted of taking the median of all the parameters found from our two-limb retrieval of the HAT-P-41b *HST* data — i.e., the medians presented in the second column of Table 3 — and use the corresponding limb models implied by them to simulate a single *JWST* NIRISS/SOSS transit observation using the `catwoman` transit model introduced in this work. As in the last sub-section, we used PandExo to

Table 2. Priors and parameters used for our Section 4.2 CHIMERA atmospheric retrievals. These are composed by two limbs, one forced to be colder than the other. $U(a, b)$ below stands for a uniform distribution between a and b . For detailed discussions on each parameter, see Line et al. (2013) for the general framework and Mai & Line (2019) for the implementation of the cloud model used in this work, which is that of Ackerman & Marley (2001).

Parameter	Prior	Comment
<i>Parameters individual to each limb</i>		
T_{irr} (K)	$U(1000, 2500)$	Stellar input at top of atmosphere.
$\log_{10} C/O$	$U(-2, 0.3)$	Log C/O ratio.
$\log_{10} K_{zz}$ (cm ² /s)	$U(5, 11)$	Log-eddy diffusion coefficient.
f_{sed}	$U(0.5, 5)$	Sedimentation efficiency.
$\log_{10} P_{\text{base}}$ (bar)	$U(-6, 1.5)$	Cloud base pressure.
$\log_{10} f_{\text{cond}}$	$U(-15, -2)$	Cloud condensate mixing ratio at cloud base.
<i>Parameters common to both limbs</i>		
[M/H]	$U(-2, 3)$	Atmospheric metallicity.
f_R	$U(0.5, 1.5)$	Multiplicative factor to 10 bar “fiducial” radius.
$\log_{10} \kappa_{IR}$ (cm ² /g)	$U(-3, 0)$	T/P profile IR opacity.
$\log_{10} \gamma_1$	$U(-3, 0)$	Log visual-to-IR opacity.

estimate the per-integration lightcurve precision for this transit observation, with which we simulated 608, 53-second integrations — i.e., a 8.95-hour exposure, the recommended time-on-target for *JWST* observations, obtained using equation 3. To generate the transit models at each wavelength, we used the same transit parameters used by Wakeford et al. (2020) with the exception of the radius for each limb, for which we use the model described above. As for limb-darkening, we used the ExoCTK (Bourque et al. 2021) limb-darkening tool¹³ to compute the limb-darkening coefficients of the quadratic law for orders 1 and 2 of NIRISS/SOSS.

We tackled the analysis of these simulated lightcurves in two different ways, in order to showcase why performing inference on the limb spectra is the best way to optimally extract information about the limbs of exoplanets. The first consisted of extracting *transit* spectra from them by simply fitting these lightcurves with `batman` lightcurve models, with the same procedure explained in Section 3.1. Then, we performed two-limb retrievals on this transit spectrum using the same modified CHIMERA atmospheric retrievals described above and performed on the *HST* data. The results of that experiment are presented in the middle panel of Figure 7; posterior credibility intervals for each fitted parameter fit in the retrieval are presented in the third column of Table 3. As can be seen, these two-limb retrievals constrain much better the different limbs than the *HST* data, but still have a fairly large uncertainty, such that the retrieved limb spectra overlaps between the limbs at certain wavelengths. While the posteriors for most parameters are fairly wide (mainly due to the cloudy nature of this particular exoplanet), the temperature posterior distribution is much better constrained than the corresponding one for the *HST* data: they have uncertainties that are about 1 to 2-fold smaller for the cold limb and about 2 to 5-fold smaller for the hot limb.

Next, we performed the transit fitting using our `catwoman` model, again, using the same procedures as the ones outlined in Section 3.1; this allowed us to extract *limb spectra directly from the transit lightcurves*. In order to perform retrievals on these limb spectra, however, we had to slightly modify the log-likelihood of our retrievals because, as explained in the previous sub-section, for each wavelength bin the two limb depths are strongly correlated. We characterize the posterior distributions of the limb depths at each wavelength bin in our simulations as multivariate gaussians, and thus compute the covariance matrix Σ_w and mean vectors

¹³ https://exoctk.stsci.edu/limb_darkening

$\vec{\mu}_w = [\delta_{1,w}, \delta_{2,w}]$ for each wavelength w . With this, the log-likelihood we use in our retrievals is given by:

$$\ln \mathcal{L} = -\frac{1}{2} \sum_w 2 \ln 2\pi + \ln |\Sigma_w| + \vec{r}_w^T \Sigma_w^{-1} \vec{r}_w$$

with $\vec{r}_w = \vec{\mu}_w - \vec{m}_w$ being the vector of residuals, with \vec{m}_w being the vector containing the model limb spectra at the given wavelength bin w .

The results of performing the retrieval on the limb spectra directly using the framework described above are presented in the bottom panel of Figure 7; posterior credibility intervals for each fitted parameter fit in the retrieval are presented in the fourth column of Table 3. As can be observed, the constraints on the limb spectra are much better than the ones obtained from fitting the transit spectra. The corresponding limb spectral models are much better differentiated by our retrievals, allowing us to tightly constrain any features that might arise in them. The temperature posteriors for the limbs are also much better constrained; in particular, there is a 2 to 4-fold precision increase on the temperature of the cold limb, and 3 to 8-fold precision increase in the hot limb when compared against the *HST* data. These results showcase that extracting and analyzing limb spectra directly allows us to constrain much more tightly the properties of the limbs than methods that rely on extracting this information from “classic” transit spectra.

Aside from impacting directly on inferences made with atmospheric retrievals, as has been shown above, we would like to highlight that extracting limb spectra directly from transit lightcurves has an additional, unique benefit: it opens up the discovery space for atmospheric features that might be individual to each of the limbs. This, in turn, has the benefit of allowing a direct comparison against Global Circulation Models (GCM). GCM modeling assumptions and implementation details have been actively driven by observations in the past few years. For instance, until recently clouds and hazes were typically added in a post-processing stage, not including feedback from these components in the modeling. Recent works such as those of Roman & Rauscher (2019) and Parmentier et al. (2020) have managed to implement clouds in their GCMs directly, showing in turn that this is critical to understand the overall cloud structure itself and heat redistribution in the planets under study, which has provided a much better match to observed phase-curve observations. We believe the study of limb spectra can open up a similar set of insights providing key advancements in the overall modeling of exoplanetary atmospheres.

From an observational perspective, it is interesting to consider that observations aiming to extract these limb

spectra can be much cheaper than, e.g., phase-curves. Whereas a single NIRISS/SOSS transit for HAT-P-41b, for instance, would amount to a total science time to a *JWST* proposal of about 8.95 hours (using Equation 3), a full phase-curve for this particular exoplanet requires over 65 hours. In this sense, extraction of limb spectra could serve as a good diagnostic as to what to expect in a phase-curve observation *before* performing these expensive observations. Since for a fixed planetary and stellar radii the ingress/egress duration increases with the square-root of the semi-major axis (i.e., $\tau \propto \sqrt{a}$), this technique for detecting limb asymmetries might in turn be an excellent alternative avenue to studying morning and evenings of longer period planets where phase-curve signals are too small to be detectable in a reasonable amount of time.

4.3. Timing variation biases due to asymmetric terminator depths

In Section 3 we discussed how, as predicted by von Paris et al. (2016), small changes in the time-of-transit center can give rise to equally good fits on symmetric models (such as the ones assumed by the `batman` package, for instance), even if the data is truly arising from an asymmetric transit model (although this limitation can be bypassed if the aim is to retrieve limb spectra by simultaneously fitting transit lightcurves at different wavelengths; see, e.g., Powell et al. 2019). It is important to note that this in turn can give rise to biases in transit times if a symmetric model is used when the data in fact comes from an asymmetric model such as the one modeled by the `catwoman` library. In our simulations, these can give rise to timing offsets of up to 5 seconds, which is in turn within the timing precision that the *TESS* mission is able to reach, and will be for sure within reach of the *JWST* mission. Care must be taken, thus, when searching for small (second-level) timing offsets in these precise transit lightcurves in the search of, e.g., transit timing variations.

4.4. Limitations of this study

It is important to note that throughout this work, we have assumed that the only alternative model to that of limb asymmetries is that of a symmetric limb in order to explain transit lightcurves asymmetries. However, there are other competing effects that might give rise to asymmetric lightcurves as well. For instance, known stellar effects such as gravity darkening (see, e.g., Ahlers et al. 2020, and references therein) and yet-to-be uncovered effects/properties such as exoplanetary rings (see, e.g., Rein & Ofir 2019, and references therein) can also give rise to asymmetric lightcurves. Performing a detailed

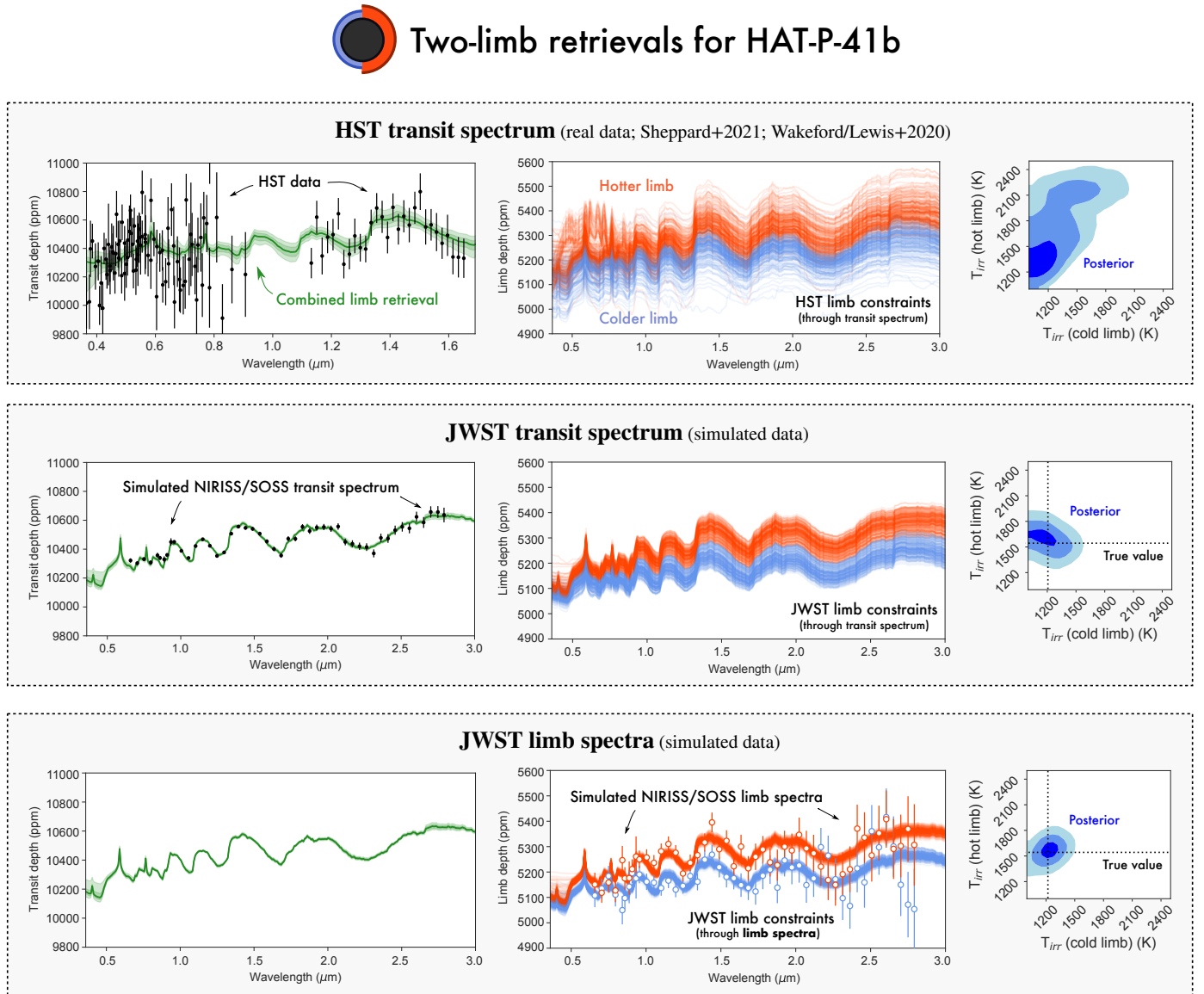


Figure 7. Two-limb retrievals made on real *HST* and simulated *JWST* data. (Top) Observed transit spectrum by *HST* STIS ($< 1.0 \mu\text{m}$) and *HST* WFC3/IR ($> 1.0 \mu\text{m}$; black points with errorbars) of HAT-P-41b presented in Wakeford et al. (2020), Lewis et al. (2020) and Sheppard et al. (2021), along with the retrieved transit spectrum (left; green bands representing the 68% and 95% credibility intervals), 200 random draws from the posterior retrieved limb models (middle) and posterior distribution of the temperatures of those limbs (right). (Middle) Same, but for two-limb retrievals made on a simulated *JWST* NIRISS/SOSS transit spectrum. (Bottom) Same, but for a retrieval made on the *limb spectra*, extracted directly from simulated transit lightcurves. See text for details. **Main point:** Retrievals made directly on limb spectra (bottom panel) constrain much better the limb models than retrievals made on “classic” transit spectra (top and middle panels).

Table 3. Posterior credibility intervals (C.I.) of the two-limb retrieval made on real *HST* data and simulated *JWST/NIRISS* data of HAT-P-41b. C.I. below correspond to medians and 68% credibility bands around it. For details on the definition for each parameter and priors, see Table 2.

Parameter	Posterior C.I. (transit spectrum, <i>HST</i>)	Posterior C.I. (transit spectrum, <i>JWST</i> ^a)	Posterior C.I. (limb spectra, <i>JWST</i> ^a)
<i>Parameters for the “cold” limb</i>			
T_{irr} (K)	1210^{+227}_{-132}	1197^{+130}_{-115}	1237^{+59}_{-70}
$\log_{10} C/O$	$-0.85^{+0.56}_{-0.65}$	$-0.98^{+0.42}_{-0.57}$	$-0.99^{+0.42}_{-0.56}$
$\log_{10} K_{zz}$ (cm ² /s)	$7.9^{+1.7}_{-1.6}$	$8.0^{+1.9}_{-1.9}$	$7.7^{+1.9}_{-1.7}$
f_{sed}	$3.4^{+1.6}_{-1.7}$	$3.4^{+1.6}_{-1.7}$	$3.3^{+1.8}_{-1.7}$
$\log_{10} P_{\text{base}}$ (bar)	$-2.1^{+1.9}_{-1.9}$	$-1.9^{+2.1}_{-2.5}$	$-1.8^{+2.1}_{-2.6}$
$\log_{10} f_{\text{cond}}$	$-7.0^{+3.1}_{-4.5}$	$-9.3^{+3.6}_{-3.5}$	$-9.2^{+3.9}_{-3.5}$
<i>Parameters for the “hot” limb</i>			
T_{irr} (K)	1522^{+519}_{-241}	1592^{+94}_{-108}	1567^{+66}_{-76}
$\log_{10} C/O$	$-0.68^{+0.50}_{-0.78}$	$-1.16^{+0.49}_{-0.52}$	$-1.23^{+0.51}_{-0.48}$
$\log_{10} K_{zz}$ (cm ² /s)	$8.0^{+1.7}_{-1.7}$	$7.8^{+2.0}_{-1.8}$	$7.8^{+2.1}_{-1.8}$
f_{sed}	$3.1^{+1.6}_{-1.5}$	$3.3^{+1.7}_{-1.6}$	$3.3^{+1.7}_{-1.7}$
$\log_{10} P_{\text{base}}$ (bar)	$-2.5^{+2.0}_{-1.9}$	$-1.9^{+2.1}_{-2.5}$	$-1.9^{+2.1}_{-2.5}$
$\log_{10} f_{\text{cond}}$	$-8.0^{+3.8}_{-4.0}$	$-9.1^{+3.7}_{-3.6}$	$-9^{+3.8}_{-3.7}$
<i>Parameters common to both limbs</i>			
[M/H]	$2.06^{+0.24}_{-0.37}$	$2.02^{+0.036}_{-0.041}$	$2.022^{+0.037}_{-0.039}$
f_R	$1.0276^{+0.0072}_{-0.0087}$	$1.0273^{+0.0017}_{-0.0027}$	$1.0276^{+0.0014}_{-0.0022}$
$\log_{10} \kappa_{IR}$ (cm ² /g)	$-2.23^{+0.51}_{-0.50}$	$-1.92^{+0.75}_{-0.61}$	$-2.32^{+0.57}_{-0.43}$
$\log_{10} \gamma_1$	$-1.57^{+0.72}_{-0.81}$	$-1.74^{+0.77}_{-0.75}$	$-1.76^{+0.95}_{-0.80}$

^aThe *JWST* simulations had as underlying true values the medians from our *HST* retrievals.

model comparison study between these effects and the one studied here is out the scope of this work, but we warn researchers that proper care must be taken when aiming to claim the detection of asymmetric limbs in light of these possibilities. While effects like, e.g., gravity darkening are most likely known at good enough precisions in order to understand when a given transit lightcurve might be asymmetric due to this effect or at the very least to put limits on asymmetries generated by it, known unknowns such as exoplanetary rings might be more complicated to rule out. Perhaps the easiest way to constrain this would be through the wavelength-dependence of these asymmetries, which we hypothesise should be markedly different in the case of exoplanetary rings and those produced by opacity sources in an exoplanetary atmosphere. Still, it is important to be mindful of these alternative hypotheses when analyzing data on the search of these lightcurve asymmetries.

In addition to the above, the very validity of the framework developed here — i.e., fitting transit lightcurves with a model of two “stacked”, rotated semi-circles — remains to be put to the test with real data, and has plenty of room for improvement as we increase the precision of our measurements. For instance, our model assumes a sharp discontinuity at the poles, whereas some GCMs actually predict smooth transitions at them (see, e.g., Pluriel et al. 2020, and references therein), even suggesting morning and evening terminators might be *themselves* asymmetric. While a path in the right direction, our model is just an approximation to reality by construction, as those simplifications were the ones that allowed us to create a modeling scheme that is fast and efficient to apply to real transit lightcurve data. We expect that the detection of the signatures of mornings and evenings on actual, precise transit lightcurves from *TESS* or *JWST* could indeed motivate more flexible and accurate models for their shapes guided by GCM modeling (or the data themselves) that could expand on the simple modeling scheme discussed in this work. While these shapes might be complex enough that simple geometrical arguments like the ones made in this work would most likely not be easy to make, making the problems hard to parametrize, we are hopeful that good ideas might flourish in the exoplanet community to make this happen. There currently exists a continuum of lightcurve analysis methods ranging from few-number-of-parameter but constrained models like ours to very flexible but large-number-parameter models like the shadow imaging technique presented in Sandford & Kipping (2019). We believe expanding our model in the direction discussed above lies in between those methodologies, and is thus

bounded — and therefore approachable. Developing this idea further, however, is outside the scope of this work.

5. CONCLUSIONS

In this work, we have presented a detailed study on the observational prospects of directly detecting transit lightcurve asymmetries due to inhomogeneous exoplanetary limbs with current and near-future instrumentation. A semi-analytical framework was introduced in Section 2 to fit transit lightcurves in order to extract the transit depths of the different limbs, a problem which is approximated as a pair of stacked semi-circles of different radii transiting a limb-darkened star following von Paris et al. (2016). Implemented in the `catwoman` python library (Jones & Espinoza 2020), this framework allows for the fast computation of these lightcurves, which are even able to model the rotation of the axis that joins the semi-circles, being thus able to characterize sky-projected planetary spin-orbit misalignments in a complementary fashion to that allowed by the eclipse mapping technique for both lightcurves (Rauscher et al. 2007; Williams et al. 2006) and radial-velocities (Nikolov & Sainsbury-Martinez 2015).

A detailed feasibility study was presented in Section 3 for detecting the effect with current existing facilities such as *TESS* and near-future observatories such as *JWST*. Even in a worst-case scenario of a planetary transit with a very small ingress/egress duration (which is the portion of the lightcurve that mainly constrains the limbs), the prospects for detecting the effect are very promising, even considering our ignorance on the angle that defines the sky-projected planetary spin-orbit misalignment. If aiming at detecting the effect with only one transit, however, care must be taken as the time of transit center is highly degenerate with the limb asymmetries (i.e., a small shift in the time-of-transit can give rise to a similarly good fit to that of an asymmetric lightcurve due to inhomogeneous limbs).

Finally, we showed in Section 4 how important the transit ingress/egress duration is for the detection of the effect. We used HAT-P-41b as a case-study to showcase the prospects for extracting the spectra of each of its limbs, and concluded that analyzing the lightcurves directly with the methods presented in this work might be one of the most efficient ways to obtain a global picture of each of the limbs, with *JWST*-like precisions enabling the extraction of their spectra given the exquisite spectrophotometric precision the observatory will be able to achieve.

We believe the promise of being able to characterize the limbs of exoplanets could play a pivotal role in our understanding of the 3-dimensional structure of exo-

planets, and could provide observations that can inform current (e.g., GCM, transmission spectroscopy models) and future (e.g., phase-curves) models and observations aimed at the characterization of exoplanet atmospheres. The technique might, in turn, be a much less time-demanding technique to probe the 3D structure of longer period exoplanets, where phase-curves can be prohibitively expensive. Overall, we believe exploring the detectability of the effect in real transit lightcurves is critical to understand the limitations of the technique of transit spectroscopy when it comes to interpreting structural profiles such as temperature/pressure profiles and abundances in a 1-dimensional fashion (MacDonald et al. 2020). This, in turn, will be fundamental to make claims regarding formation mechanisms of these exoplanets based on the latter (Öberg et al. 2011; Espinoza et al. 2017; Mordasini et al. 2016), and their overall dependence with planetary properties (see, e.g., Sing et al. 2016; Welbanks et al. 2019, and references therein).

ACKNOWLEDGMENTS

We would like to thank the anonymous referee for their excellent feedback which significantly improved the presentation of our results.. We would also like to thank L. Carone and P. Mollière for fruitful discussions on the theory of transmission spectroscopy and 3D modeling as applied to asymmetric limbs, as well as L. Kreidberg, T. Louden, D. Powell and N. Nikolov on fruitful discussions regarding constraining limb inhomogeneities directly from transit lightcurves. N.E. would like to thank the IAU and the Gruber foundation for the support to this research through the IAU-Gruber Fellowship, with which this work was started. Finally, we would also like to thank the MPIA Summer Program for the support to start this research.

APPENDIX

A. DERIVING ΔA

In order to derive the decrement of flux due to the transit of a pair of stacked semi-circles given by equation 1, we must find ΔA , the inter-sectional area between the stacked semi-circles and the iso-intensity band depicted in Figure 1. As already noted by Kreidberg (2015) in the case of a circle, this area is simply the inter-sectional area of the stacked semi-circles with the circle of radius x_i , $A(x_i, R_{p,1}, R_{p,2}, d, \varphi)$, minus the same inter-sectional area but with the circle of radius x_{i-1} , $A(x_{i-1}, R_{p,1}, R_{p,2}, d, \varphi)$, i.e.,

$$\Delta A = A(x_i, R_{p,1}, R_{p,2}, d, \varphi) - A(x_{i-1}, R_{p,1}, R_{p,2}, d, \varphi).$$

This implies that to find ΔA one has to first find a general form for the inter-sectional area between the stacked semi-circles and a circle. These stacked semi-circles, in turn, are composed of two semi-circles, and thus the problem reduces to calculating the area of the intersection between a circle and two (rotated) *semi-circles* with a common center: one of radius $R_{p,1}$ and another of radius $R_{p,2}$, but rotated by 180 degrees. Given a general formula for such intersection, $A_S(R, R_S, d, \theta)$, where R is the radius of the circle, R_S the radius of the semi-circle, d the distance between the center of the circle and the semi-circle and θ the rotation angle of the semi-circle with respect to d , then

$$A(x, R_{p,1}, R_{p,2}, d, \varphi) = A_S(x, R_{p,1}, d, \varphi) + A_S(x, R_{p,2}, d, \varphi + \pi).$$

If we find a general form for $A_S(\cdot)$, then we solve the problem. We tackle this problem in the next sub-section.

A.1. Intersection area between a circle and a semi-circle

Although the case of calculating the intersection area between two circles can be obtained via elemental trigonometry, the problem of calculating the intersection area between a circle and a (rotated) *semi-circle* is not, in general, as straightforward.

We first note that the problem of finding the intersection area of a circle of radius R and a semi-circle of radius R_S rotated by an angle θ with respect to the line that joins the centers of length d is the same problem as the intersection area of a semi-circle and a *circle rotated by an angle θ with respect to the line that joins the centers*. This symmetry argument allows us to put the horizontal axis of this problem in the base of the semi-circle, simplifying the notation of the problem. Without loss of generality, we put the origin in the center of the base of the semi-circle. This transformed geometry of the problem is shown in Figure 8; here the white dashed area inside the semi-circle is the area of interest (i.e., the one that leads to $A_S(R, R_S, d, \theta)$).

As is evident in Figure 8, there are three different cases (a, b and c) we have to take care of in order to find a general formula for $A_S(R, R_S, d, \theta)$:

- Case (a), divided into sub-cases (a-1), (a-2) and (a-3), deals with the problem in which the circle is rotated such that it lies above the semi-circle. If we identify the coordinates of the center of the circle as $(x_0, y_0) = (-d \cos \theta, d \sin \theta)$, case a) deals with the problem in which $\theta > 0$ and, thus, $d \sin \theta > 0$. Here, the intersection points between the circle and the semi-circle have coordinates (a_1, b_1) and (a_2, b_2) . The geometry depicted in Figure 8 for this case implies that $b_1 = 0$. This is because for $b_1 > 0$, the problem is the same as the intersection of two circles (one of radius R and another of radius R_S), which has a known analytical solution (see, e.g., Kreidberg 2015). Here the area of interest, A_S , is given by the area of the semi-circle ($\pi R_S^2/2$) minus $A_1 + A_2$ for case (a-1) and by $A_1 + A_2 + A_3$ for cases (a-2) and (a-3). The different sub-cases depend, in turn, on the location of the intersection points and the position of (a_3, b_3) , the position of the maximum extension of the circle in the x-axis.
- Case (b) deals with the problem in which the circle is rotated such that it lies *below* the semi-circle, i.e., where $\theta < 0$ and, thus, $d \sin \theta < 0$. In addition, this case handles only problems in which one intersection of the circle with the semi-circle is in its base and the other is with the upper part of the semi-circle. Once again, the intersection points between the circle and the semi-circle have coordinates (a_1, b_1) and (a_2, b_2) . In this case, however, $b_2 = 0$; the cases in which $b_2 \neq 0$ (i.e., when the right-most intersection is on the upper part of the semi-circle) and in which $b_2 = 0$ and $b_1 = 0$ (i.e., in which the left-most intersection is also on the base of the semi-circle) is taken care of by case c). The area of interest for case (b) is $A_S = A_1 + A_2$.
- Finally, case (c), divided into sub-cases (c-1), (c-2) and (c-3), deals with the problem in which the circle is either rotated above or below the semi-circle, but where there are two intersections with both either in the base (c-1) or in the upper part of the semi-circle (c-2) or four intersection points (c-3) between the circle and the semi-circle. In this case, the area of interest, A_S can be calculated directly via basic trigonometry and thus we don't identify here the intersection points by coordinates but by the red points in order to guide the reader.

Cases (a), (b) and (c) defined above will all be calculated assuming that the center of the circle is to the left of the semi-circle. The reason for doing this is that the problem has reflective symmetry with respect to the line that goes through the center of the semi-circle and that is perpendicular to its base. As such, for $0 < \theta < \pi/2$ we have that $A_S(R, R_S, d, \theta) = A_S(R, R_S, d, \pi - \theta)$, whereas for $-\pi/2 < \theta < 0$, $A_S(R, R_S, d, \theta) = A_S(R, R_S, d, \theta - \pi)$. In what follows, we solve each of the cases separately.

A.1.1. Case (a)

Before looking at the integrals that lead to the intersection area between the circle and the semi-circle in this case, let us obtain the expressions for the intersection points (a_1, b_1) and (a_2, b_2) . To do this, we first note that the point where the circle intersects with the line $y = 0$ (which is the line that passes through the base of the semi-circle) is given by

$$x_{\text{int}} = -d \cos \theta \pm \sqrt{R^2 - d^2 \sin^2 \theta}. \quad (\text{A1})$$

If the discriminant of this expression is negative (or zero), which in this case implies that $|d \sin \theta| \geq R$, then there is no (or one) intersection of the circle with the x-axis. In this case, the intersectional area can either be zero if $d \geq R + R_S$ or equal to solving the problem of the intersection between two circles of radius R and R_S in the case in which $d < R + R_S$. If the latter case is true, in turn, the intersectional area reduces to πR^2 when $d + R < R_S$ (i.e., when the circle is inside the semi-circle).

If $|d \sin \theta| < R$, then we have two solutions for the intersection points of the circle and the x-axis, x_{int} . The cases in which both solutions are inside the semi-circle, i.e., when $|x_{\text{int}}| \leq R_S$, will be handled in case (c), as depicted in Figure 8. If both solutions are *outside* the semi-circle, i.e., when $|x_{\text{int}}| > R_S$, there are two possibilities. If $d \geq R + R_S$, the intersection area is zero — in this case, the circle is always to the left of the semi-circle. If, on the other hand, $d < R + R_S$, then because the intersections with the x-axis happen outside the semi-circle, there are two options: either the circle intersects twice with the upper part of the semi-circle (a case that will be solved in case (c-2)) or the circle covers all of the semi-circle, in which case the intersectional area is $\pi R_S^2/2$. If $\theta > 0$, then this leaves us,

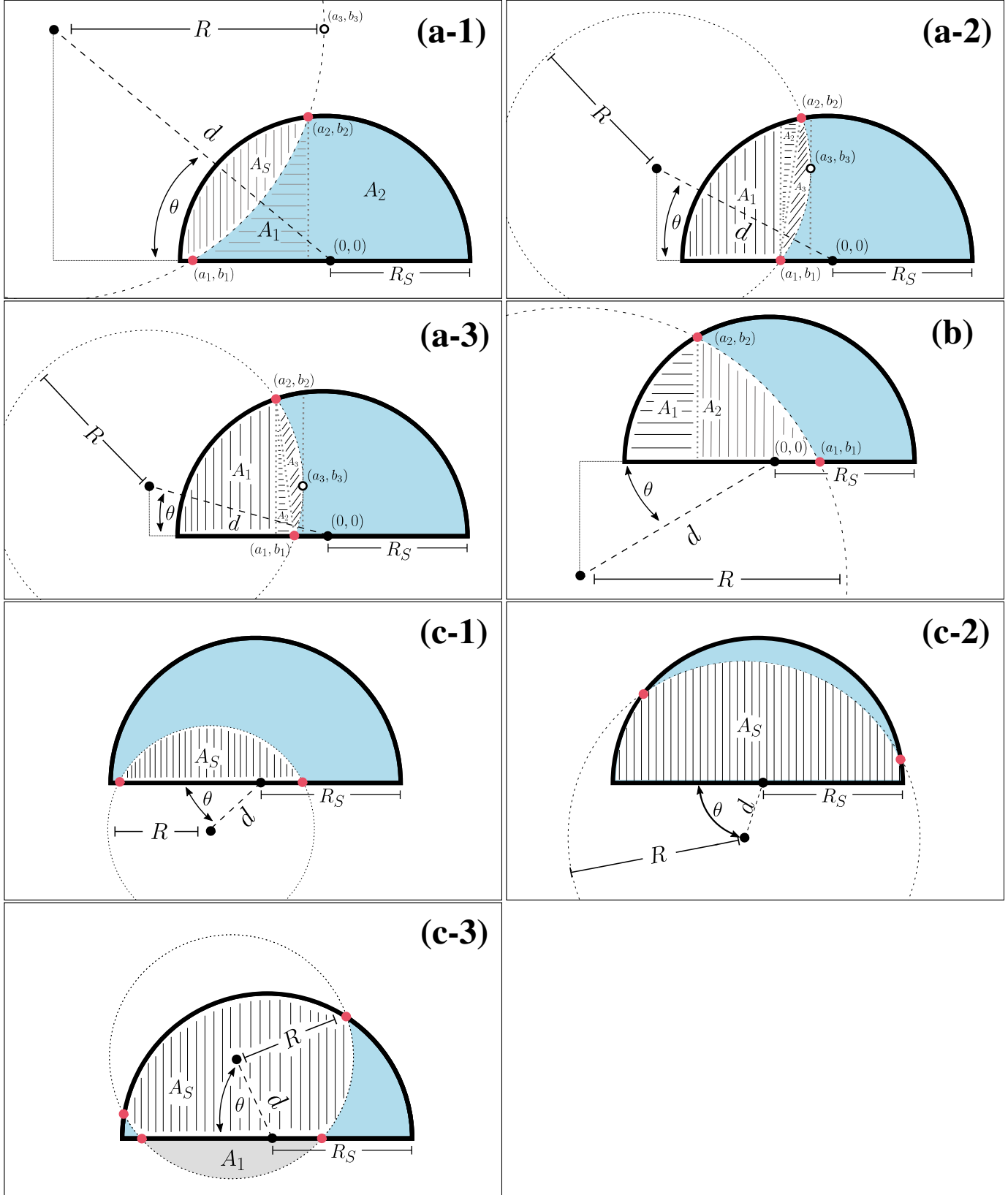


Figure 8. Transformed geometry of the problem — we chose to rotate the circle of radius R around the semi-circle of radius R_S by an angle θ . This problem is the same as having the semi-circle rotated with respect to the line that joins the centers (of length d) by an angle θ . The general problem can, in turn, be divided in three cases: (a) when the center of the circle is above the base of the semi-circle (divided, in turn, in sub-cases a-1, a-2 and a-3), (b) when the center of the circle is below the base of the semi-circle and the intersection points are not both touching the base or the edge of the semi-circle and (c) when there are two (c-1) or more (c-2) simultaneous intersection points with either at the edge or at the base of the semi-circle; this latter case can be solved using basic trigonometry. In all cases, the intersection points between the semi-circle and the circle are indicated by red dots. In all cases, the area of interest is the white dashed one inside the semi-circles.

finally, with the problem we will solve for case (a) (is this is not true then case (b) will apply), in which x_{int} has both one solution outside and another one inside the semi-circle. Because here we are dealing with the cases in which the center of the circle is always to the left of the center of the semi-circle, this implies that the intersection point inside the semi-circle will always be the right-most intersection point, i.e., the solution of x_{int} with the positive sign. In the notation of Figure 8, this gives the intersection points

$$a_1 = -d \cos \theta + \sqrt{R^2 - d^2 \sin^2 \theta},$$

$$b_1 = 0.$$

The intersection point between the upper part of the semi-circle and the circle, (a_2, b_2) , is obtained by simply equating the equation of the circle $((x + d \cos \theta)^2 + (y - d \sin \theta)^2 = R^2)$ with the equation of the semi-circle, taking it as a full circle $(x^2 + y^2 = R_S^2)$ to begin with. This yields

$$b_2 = -A \sin \theta + \cos \theta \sqrt{R_S^2 - A^2}, \quad (\text{A2})$$

$$a_2 = b_2 \tan \theta + \frac{A}{\cos \theta}, \quad (\text{A3})$$

where

$$A = \frac{R^2 - R_S^2 - d^2}{2d}.$$

As we are not dealing with two intersecting circles, but an intersecting circle and semi-circle, we have chosen the largest b_2 which will give rise to the a_2 , and therefore the point of intersection, that is on the semi-circle.

Finally, an important set of coordinates to define are the ones for (a_3, b_3) . As illustrated in Figure 8, these are the coordinates of the maximum value attained in the x-axis by the circle. The coordinates for this point are, evidently,

$$a_3 = -d \cos \theta + R,$$

$$b_3 = d \sin \theta.$$

First, we take on **case (a-1)**. This case occurs when the conditions for case (a) are met and when the point (a_3, b_3) is *outside* the semi-circle, which in turn implies in this case that $b_3 \geq b_2$. To solve it, the strategy to obtain A_S is to compute analytic solutions to the areas A_1 and A_2 depicted in Figure 8, and then subtract these to $\pi R_S^2/2$. First, A_1 is simply the area under the curve of the circle from $x = a_1$ to $x = a_2$. Because in this case $a_1 < a_2 < a_3$, we are going to integrate the lower part of the circle; this implies the equation of the (in this case semi) circle is simply

$$y = -\sqrt{R^2 - (x + d \cos \theta)^2} + d \sin |\theta|.$$

Integrating this from $x = a_1$ to $x = a_2$ yields

$$A_1 = \frac{R^2}{2} \Delta f + d \sin |\theta| (a_2 - a_1), \quad (\text{A4})$$

where $\Delta f = f(a_1) - f(a_2)$, with

$$f(x) = \left(\frac{x + d \cos \theta}{R^2} \right) \sqrt{R^2 - (x + d \cos \theta)^2} + \arcsin \left(\frac{x + d \cos \theta}{R} \right).$$

Next, we work on obtaining area A_2 . This is simply the area under the curve of the semi-circle, whose equation is $y = \sqrt{R_S^2 - x^2}$. Integrating this from $x = a_2$ to $x = R_S$ yields

$$A_2 = \frac{R_S^2}{2} \left[\frac{\pi}{2} - h(a_2) \right], \quad (\text{A5})$$

where

$$h(x) = \arcsin \left(\frac{x}{R_S} \right) + \frac{x}{R_S} \sqrt{1 - \frac{x^2}{R_S^2}}.$$

Thus using the definitions for A_1 given in equation (A4) and for A_2 given in equation (A5), area A_S is given in this case by

$$A_S = \frac{\pi R_S^2}{2} - \frac{R^2}{2} \Delta f - d \sin |\theta| (a_2 - a_1) - \frac{R_S^2}{2} \left[\frac{\pi}{2} - h(a_2) \right].$$

Now, we take on **case (a-2)**. In this case $b_3 < b_2$, however, $a_2 > a_1$. In this case, the area of interest is $A_S = A_1 + A_2 + A_3$, as depicted in Figure 8. First, area A_1 in this case is the area of the semi-circle from $x = -R_S$ to $x = a_1$. Integrating once again the equation of the semi-circle ($y = \sqrt{R_S^2 - x^2}$) in this range one obtains

$$A_1 = \frac{R_S^2}{2} \left[h(a_1) + \frac{\pi}{2} \right]. \quad (\text{A6})$$

Area A_2 in this case can be calculated as the area under the same semi-circle between $x = a_1$ and $x = a_2$ *minus* $b_2(a_2 - a_1)/2$, which is the area of the triangle formed between the points (a_1, b_1) , (a_2, b_2) and $(a_2, 0)$. Integrating the semi-circle between $x = a_1$ and $x = a_2$ and subtracting $b_2(a_2 - a_1)/2$, we obtain

$$A_2 = \frac{R_S^2}{2} [h(a_2) - h(a_1)] - \frac{b_2(a_2 - a_1)}{2}. \quad (\text{A7})$$

Finally, area A_3 reduces to obtaining the segment of a circle generated by drawing a chord between points (a_1, b_1) and (a_2, b_2) . To this end, we ought to know the angle α (in radians) these points make with respect to the center of the circle. This can be easily obtained by the Law of Cosines to give

$$\alpha = \arccos \left(1 - \frac{(a_2 - a_1)^2 + b_2^2}{2R^2} \right).$$

With this, the area of the segment A_3 is thus, simply

$$A_3 = \frac{R^2}{2} (\alpha - \sin \alpha). \quad (\text{A8})$$

Finally, then, using the definition for A_1 in equation (A6), for A_2 in equation (A7) and for A_3 in equation (A8), we get in this case

$$A_S = \frac{R_S^2}{2} \left[h(a_2) + \frac{\pi}{2} \right] - \frac{b_2(a_2 - a_1)}{2} + \frac{R^2}{2} (\alpha - \sin \alpha).$$

Finally, we solve **case (a-3)**. In this case again $b_3 < b_2$, however, $a_1 > a_2$. Here, equation (A6) also applies for A_1 , but the upper limit of the integral is in this case a_2 instead of a_1 . This implies that in this case

$$A_1 = \frac{R_S^2}{2} \left[h(a_2) + \frac{\pi}{2} \right]. \quad (\text{A9})$$

To obtain area A_2 in this case, we note that here this is simply the area of the triangle formed by the points with coordinates (a_1, b_1) , (a_2, b_2) and $(a_2, 0)$. In this case, thus,

$$A_2 = \frac{b_2(a_1 - a_2)}{2}. \quad (\text{A10})$$

Finally, to obtain A_3 we use equation (A8) which also applies for this case. Using then the definition for A_1 in equation (A9), for A_2 in equation (A10) and for A_3 in equation (A8), we get in this case

$$A_S = \frac{R_S^2}{2} \left[h(a_2) + \frac{\pi}{2} \right] + \frac{b_2(a_1 - a_2)}{2} + \frac{R^2}{2} (\alpha - \sin \alpha).$$

A.1.2. Case (b)

Case (b) is similar in many ways to case (a), with the only difference that now the coordinates of the center of the circle change to $(-d \cos \theta, -d \sin |\theta|)$, and thus some functions and integration ranges change signs. In this case, the intersection points of the circle with the x-axis are the same as the ones given in equation (A1), and thus all of the discussion given at the beginning of the past sub-section also applies for case (b). In particular, the intersection points (a_1, b_1) and (a_2, b_2) derived for case (a) are the same for this case.

In this case, the area of interest is the sum of area A_1 and A_2 . The former is the integral of the semi-circle circle from $x = -R_S$ to $x = a_2$, which is an integral which was already found in equation (A9). As for area A_2 , this is the integral of the upper part of the circle of radius R , i.e., of the function

$$y = \sqrt{R^2 - (x + d \cos \theta)^2} - d \sin |\theta|.$$

However, the integral of this from $x = a_2$ to $x = a_1$ is exactly the same integral calculated in case (a-1), whose result is on equation (A4), because the integrand there was the same integrand that we have here but multiplied by -1, and the limits of integration there were reversed with respect to the ones we have here (i.e., they went from a_1 to a_2) — because inverting the limits of integration is the same as calculating the integral multiplied by -1, both effects cancel out. Thus, area A_2 in our case is area A_1 in case (a-1). Thus, for case (b), we have that $A_S = A_1 + A_2$, i.e.,

$$A_S = \frac{R_S^2}{2} \left[h(a_2) + \frac{\pi}{2} \right] + \frac{R^2}{2} \Delta f + d \sin |\theta| (a_2 - a_1).$$

A.1.3. Case (c)

Case (c) focuses on when $|d \sin \theta| < R$, i.e. there are two solutions for the intersection points of the circle with the line $y = 0$.

More specifically, **case (c-1)** occurs also when $|x_{\text{int}}| \leq R_S$, i.e. when the two solutions for the intersection points are inside the semi-circle and when the part of the circle above the intersection points is completely enclosed within the semi-circle (see Figure 8). This can be quantitatively described by theoretically 'extending' the semi-circle into a full circle of radius R_S . The coordinates of intersection of these two circles (setting the center of the circle of radius R_S at the origin) can be found by substituting $x^2 + y^2 = R_S^2$ into $(x + d \cos \theta)^2 + (y + d \sin \theta)^2 = R^2$ to give the y coordinates:

$$y = -A \sin \theta \pm \cos \theta \sqrt{R_S^2 - A^2},$$

where

$$A = \frac{R^2 - R_S^2 - d^2}{2d}.$$

This is similar to equations A2 and A3 except the position of the circles relative to the origin have been changed slightly.

Therefore case (c-1) applies when $|x_{\text{int}}| \leq R_S$ and either:

- There is no solution for the intersection of the two circles. This will occur when $A^2 > R_S^2$.
- Both of the y-coordinate solutions are real and negative, i.e. when $-A \sin \theta \pm \cos \theta \sqrt{R_S^2 - A^2} < 0$.

Case (c-2) occurs when $|x_{\text{int}}| > R_S$ and when there are two intersection points on the curved edge of the semi-circle. For this case, the y-coordinates of intersection between the circle R and the full circle of radius R_S must be positive. Using the same equations as above, this is when $-A \sin \theta \pm \cos \theta \sqrt{R_S^2 - A^2} \geq 0$, where A is defined as in case (c-1).

Case (c-3) occurs when $|x_{\text{int}}| \leq R_S$ and when there are two further intersection points on the curved edge of the semi-circle, making a total of four intersection points. Therefore case (c-3) is when $|x_{\text{int}}| \leq R_S$ and $-A \sin \theta \pm \cos \theta \sqrt{R_S^2 - A^2} \geq 0$.

To solve case (c-1), the points of intersection in the base of the semi-circle can be obtained via equation A1:

$$x_{\text{int}}^{\pm} = -d \cos \theta \pm \sqrt{R^2 - d^2 \sin^2 \theta}.$$

The problem is then just calculating the area of the segment A_S which is a well-known geometric problem with the solution

$$A_S = R^2 \arccos\left(\frac{y}{R}\right) - xy,$$

where

$$\begin{aligned} x &= (1/2)(x_{\text{int}}^+ + |x_{\text{int}}^-|), \\ &= \sqrt{R^2 - d^2 \sin^2 \theta}, \\ y &= -d \sin \theta. \end{aligned}$$

To solve case (c-2), the problem can be set up by first theoretically 'extending' the semi-circle into a full circle of radius R_S and calculating the area of intersection of the two circles using the equations described in [Kreidberg \(2015\)](#):

$$A_{\text{int}} = R^2 \arccos u + R_S^2 \arccos v - (1/2)\sqrt{w}, \quad (\text{A11})$$

where

$$\begin{aligned} u &= (d^2 + R^2 - R_S^2)/(2dR), \\ v &= (d^2 + R_S^2 - R^2)/(2dR_S), \\ w &= (-d + R + R_S)(d + R - R_S)(d - R + R_S)(d + R + R_S). \end{aligned}$$

Using A_{int} , one can find A_S by subtracting half the area of the 'extended' circle of radius R_S to yield

$$A_S = A_{\text{int}} - \pi R_S^2/2.$$

To solve case (c-3), the problem needs to be split up into two parts. The first part involves finding the area of intersection, A_{int} , of the circle and the semi-circle 'extended' into a full circle of radius R using the same method from part (c-2) and the second involves finding area A_1 . As can be seen from the Figure 8, once these two areas are found, it is simply a matter of subtracting A_1 from A_{int} to find A_S .

To find A_1 is a very similar problem to case (c-1), the points of intersection along the base of the semi-circle can be found using equation [A1](#) and then the problem reduces to that of finding the area of a segment, which is A_1 in this case. Following a similar method for case (c-1),

$$A_1 = R^2 \arccos\left(\frac{-y}{R}\right) + xy,$$

where x and y are defined the same as for case (c-1), however note change in sign of y , due to the change of orientation of the shapes. As mentioned, A_{int} is the same as in case (c-2) and is described in equation [A11](#).

Therefore the total intersection area A_S , is given by

$$A_S = A_{\text{int}} - A_1$$

A.2. Deriving θ

In this paper we have defined θ as the angle between the base of the semi-circle and the line that extends from the base of the semi-circle to the center of the circle (of length d). Importantly, θ is defined as *positive* when extending clockwise, assuming the center of the circle is to the left of the semi-circle which, as explained in section [A.1](#), due to the symmetry of the problem, can always be achieved by flipping the frame of reference.

θ is calculated from parameters that correspond to how the system physically appears in the sky. To explain, we place the center of the star at the origin of a 2-dimensional Cartesian coordinate system. Due to the symmetry of the star, the planet is assumed to move from left to right (horizontally) across it so that the dY/dX gradient of the direction of motion of the planet at t_0 (inferior conjunction) is 0 (planet moves along the X-direction only). This

coordinate system is *different* from the frame of reference used in section A.1 when the frame is rotated so that the center of the base of the semi-circle is at the origin and the base lies along the $y=0$ axis.

θ therefore depends on the angle the semi-circle is rotated through with respect to the X-direction in the 2D system defined above, ϕ , the impact parameter, b and whether the semi-circle is originally to the left or the right of the center of the circle. The latter is characterised by the time, t and the time of inferior conjunction, t_0 and by assuming the planet moves from left to right. It is important to note that ϕ will be static if the planet moves in an almost straight line across the star (along the X-direction only). However due to orbital mechanics, the orbital path may appear curved and as such the planet will rotate slightly as it crosses the star. This rotation will perturb ϕ in such a way as discussed in A.3.

ϕ is defined in this paper between the range $-\pi/2$ to $\pi/2$, from the X-axis to the base of the *top* semi-circle, where a positive angle is defined going in the anticlockwise direction. Once this is used to find the θ for $R_{p,1}$, to obtain the θ for $R_{p,2}$, one simply has to multiply θ by -1, due to the change in direction.

Table A.2 shows how θ is calculated for the different values of ϕ , b and t for $R_{p,1}$.

t	b	ϕ	θ
$\leq t_0$	positive	$< \arccos b/d$	$-\phi - \arcsin b/d$
		$\geq \arccos b/d$	$-\pi + \phi + \arcsin b/d$
$\leq t_0$	negative	$\leq -\arccos b /d$	$\pi + \phi - \arcsin b /d$
		$> -\arccos b /d$	$-\phi + \arcsin b /d$
$> t_0$	positive	$< -\arccos b/d$	$-\pi - \phi + \arcsin b/d$
		$\geq -\arccos b/d$	$\phi - \arcsin b/d$
$> t_0$	negative	$\leq \arccos b /d$	$\phi + \arcsin b /d$
		$> \arccos b /d$	$\pi - \phi - \arcsin b /d$

A.3. Change in ϕ and the impact parameter of the semi-circle as a function of phase due to orbital mechanics

Using the same coordinate system as described in A.2, if the planet were to move in a straight line across the star, then the planet's impact parameter, b , would stay constant at the value of the impact parameter defined at t_0 (the time of inferior conjunction). From Seager (2010) this is defined as

$$b = \frac{a \cos i}{R_{\text{star}}} \left(\frac{1 - e^2}{1 - e \sin \varpi} \right), \quad (\text{A12})$$

where a is the semi-major axis, i is the inclination of the orbit, e is the eccentricity, ϖ is the longitude of periastron and R_{star} is the radius of the star. However due to the orbital motion of the planet around the star, from the perspective of our X-Y system, the orbital path of the planet is curved across the sky, and so the impact parameter becomes a function of time. For the most accurate model, b used in the equations in A.2 should be adjusted to

$$b = -r \sin(\omega + f) \cos i, \quad (\text{A13})$$

where

$$r = \frac{a(1 - e^2)}{1 + e \cos f}, \quad (\text{A14})$$

$$\cos f = \frac{\cos E - e}{1 - e \cos E}, \quad (\text{A15})$$

$$E - e \sin E = \frac{2\pi}{T}(t - t_0). \quad (\text{A16})$$

T is the orbital period of the planet, t is the current time of interest and t_0 is the time of periastron passage. The last equation can be solved numerically using a Newton-Raphson method.

Furthermore, due to the change in gradient of the planet's orbit with respect to this coordinate system, the angle between the base of the semi-circle and the X-axis will change slightly as it passes across the star. Because of how the method of deriving θ from ϕ is configured, we need this changing angle at every time-step instead of using the

original 'static' ϕ . The change in angle caused by this movement will be labelled ψ and should be added to the original ϕ to create an 'updated' ϕ_{new} . To derive ψ and make it clearer, b has been re-labelled to y , where x and y are the coordinates of this 2D system with the center of the star at (0,0). By differentiating,

$$dy = -r \cos(\varpi + f) \cos i \, df. \quad (\text{A17})$$

Also explained in Seager (2010), the x-coordinate of the center of the semi-circle will move as

$$x = -r \cos(\varpi + f), \quad (\text{A18})$$

and so

$$dx = -r \sin(\varpi + f) \, df. \quad (\text{A19})$$

Therefore ψ can be calculated from

$$\tan \psi = \frac{dy}{dx}, \quad (\text{A20})$$

$$\psi = \arctan[\cot(\varpi + f) \cos i]. \quad (\text{A21})$$

Then, ϕ should be adjusted so that

$$\phi_{new} = \phi_{old} + \psi \quad (\text{A22})$$

Software: NumPy (Harris et al. 2020), Scipy (Virtanen et al. 2020), Matplotlib (Hunter 2007), batman (Kreidberg et al. 2015), juliet (Espinoza et al. 2019), catwoman (Jones & Espinoza 2020).

REFERENCES

Ackerman, A. S., & Marley, M. S. 2001, ApJ, 556, 872, doi: [10.1086/321540](https://doi.org/10.1086/321540)

Ahlers, J. P., Johnson, M. C., Stassun, K. G., et al. 2020, AJ, 160, 4, doi: [10.3847/1538-3881/ab8fa3](https://doi.org/10.3847/1538-3881/ab8fa3)

Batalha, N. E., Mandell, A., Pontoppidan, K., et al. 2017, PASP, 129, 064501, doi: [10.1088/1538-3873/aa65b0](https://doi.org/10.1088/1538-3873/aa65b0)

Bourque, M., Espinoza, N., Filippazzo, J., et al. 2021, The Exoplanet Characterization Toolkit (ExoCTK), 1.0.0, Zenodo, doi: [10.5281/zenodo.4556063](https://doi.org/10.5281/zenodo.4556063)

Buchner, J., Georgakakis, A., Nandra, K., et al. 2014, A&A, 564, A125, doi: [10.1051/0004-6361/201322971](https://doi.org/10.1051/0004-6361/201322971)

Burrows, A., Sudarsky, D., & Hubbard, W. B. 2003, ApJ, 594, 545, doi: [10.1086/376897](https://doi.org/10.1086/376897)

Charbonneau, D., Brown, T. M., Latham, D. W., & Mayor, M. 2000, ApJL, 529, L45, doi: [10.1086/312457](https://doi.org/10.1086/312457)

Dobbs-Dixon, I., Agol, E., & Burrows, A. 2012, ApJ, 751, 87, doi: [10.1088/0004-637X/751/2/87](https://doi.org/10.1088/0004-637X/751/2/87)

Espinoza, N., Fortney, J. J., Miguel, Y., Thorngren, D., & Murray-Clay, R. 2017, ApJL, 838, L9, doi: [10.3847/2041-8213/aa65ca](https://doi.org/10.3847/2041-8213/aa65ca)

Espinoza, N., Kossakowski, D., & Brahm, R. 2019, MNRAS, 490, 2262, doi: [10.1093/mnras/stz2688](https://doi.org/10.1093/mnras/stz2688)

Feroz, F., Hobson, M. P., & Bridges, M. 2009, MNRAS, 398, 1601, doi: [10.1111/j.1365-2966.2009.14548.x](https://doi.org/10.1111/j.1365-2966.2009.14548.x)

Fortney, J. J. 2005, MNRAS, 364, 649, doi: [10.1111/j.1365-2966.2005.09587.x](https://doi.org/10.1111/j.1365-2966.2005.09587.x)

Fortney, J. J., Shabram, M., Showman, A. P., et al. 2010, ApJ, 709, 1396, doi: [10.1088/0004-637X/709/2/1396](https://doi.org/10.1088/0004-637X/709/2/1396)

Greene, T. P., Line, M. R., Montero, C., et al. 2016, ApJ, 817, 17, doi: [10.3847/0004-637X/817/1/17](https://doi.org/10.3847/0004-637X/817/1/17)

Harris, C. R., Millman, K. J., van der Walt, S. J., et al. 2020, Nature, 585, 357, doi: [10.1038/s41586-020-2649-2](https://doi.org/10.1038/s41586-020-2649-2)

Helling, C., Kawashima, Y., Graham, V., et al. 2020, A&A, 641, A178, doi: [10.1051/0004-6361/202037633](https://doi.org/10.1051/0004-6361/202037633)

Henry, G. W., Marcy, G. W., Butler, R. P., & Vogt, S. S. 2000, ApJL, 529, L41, doi: [10.1086/312458](https://doi.org/10.1086/312458)

Hubbard, W. B., Fortney, J. J., Lunine, J. I., et al. 2001, ApJ, 560, 413, doi: [10.1086/322490](https://doi.org/10.1086/322490)

Hunter, J. D. 2007, Computing in Science & Engineering, 9, 90, doi: [10.1109/MCSE.2007.55](https://doi.org/10.1109/MCSE.2007.55)

Jones, K., & Espinoza, N. 2020, Journal of Open Source Software, 5, 2382, doi: [10.21105/joss.02382](https://doi.org/10.21105/joss.02382)

Kempton, E. M. R., Bean, J. L., & Parmentier, V. 2017, ApJL, 845, L20, doi: [10.3847/2041-8213/aa84ac](https://doi.org/10.3847/2041-8213/aa84ac)

Kipping, D. M. 2013, MNRAS, 435, 2152, doi: [10.1093/mnras/stt1435](https://doi.org/10.1093/mnras/stt1435)

Kreidberg, L. 2015, PASP, 127, 1161, doi: [10.1086/683602](https://doi.org/10.1086/683602)

—. 2018, Exoplanet Atmosphere Measurements from Transmission Spectroscopy and Other Planet Star Combined Light Observations, 100, doi: [10.1007/978-3-319-55333-7_100](https://doi.org/10.1007/978-3-319-55333-7_100)

Kreidberg, L., Line, M. R., Bean, J. L., et al. 2015, ApJ, 814, 66, doi: [10.1088/0004-637X/814/1/66](https://doi.org/10.1088/0004-637X/814/1/66)

Lewis, N. K., Wakeford, H. R., MacDonald, R. J., et al. 2020, ApJL, 902, L19, doi: [10.3847/2041-8213/abb77f](https://doi.org/10.3847/2041-8213/abb77f)

Line, M. R., & Parmentier, V. 2016, ApJ, 820, 78, doi: [10.3847/0004-637X/820/1/78](https://doi.org/10.3847/0004-637X/820/1/78)

Line, M. R., Wolf, A. S., Zhang, X., et al. 2013, ApJ, 775, 137, doi: [10.1088/0004-637X/775/2/137](https://doi.org/10.1088/0004-637X/775/2/137)

MacDonald, R. J., Goyal, J. M., & Lewis, N. K. 2020, ApJL, 893, L43, doi: [10.3847/2041-8213/ab8238](https://doi.org/10.3847/2041-8213/ab8238)

Mai, C., & Line, M. R. 2019, ApJ, 883, 144, doi: [10.3847/1538-4357/ab3e6d](https://doi.org/10.3847/1538-4357/ab3e6d)

Mandel, K., & Agol, E. 2002, ApJL, 580, L171, doi: [10.1086/345520](https://doi.org/10.1086/345520)

Mordasini, C., van Boekel, R., Mollière, P., Henning, T., & Benneke, B. 2016, ApJ, 832, 41, doi: [10.3847/0004-637X/832/1/41](https://doi.org/10.3847/0004-637X/832/1/41)

Nikolov, N., & Sainsbury-Martinez, F. 2015, ApJ, 808, 57, doi: [10.1088/0004-637X/808/1/57](https://doi.org/10.1088/0004-637X/808/1/57)

Öberg, K. I., Murray-Clay, R., & Bergin, E. A. 2011, ApJL, 743, L16, doi: [10.1088/2041-8205/743/1/L16](https://doi.org/10.1088/2041-8205/743/1/L16)

Parmentier, V., Showman, A. P., & Fortney, J. J. 2020, arXiv e-prints, arXiv:2010.06934. <https://arxiv.org/abs/2010.06934>

Pluriel, W., Zingales, T., Leconte, J., & Parmentier, V. 2020, A&A, 636, A66, doi: [10.1051/0004-6361/202037678](https://doi.org/10.1051/0004-6361/202037678)

Pontoppidan, K. M., Pickering, T. E., Laidler, V. G., et al. 2016, Society of Photo-Optical Instrumentation Engineers (SPIE) Conference Series, Vol. 9910, Pandeia: a multi-mission exposure time calculator for JWST and WFIRST, 991016, doi: [10.1117/12.2231768](https://doi.org/10.1117/12.2231768)

Powell, D., Louden, T., Kreidberg, L., et al. 2019, arXiv e-prints, arXiv:1910.07527. <https://arxiv.org/abs/1910.07527>

Rauscher, E., Menou, K., Seager, S., et al. 2007, ApJ, 664, 1199, doi: [10.1086/519213](https://doi.org/10.1086/519213)

Rein, E., & Ofir, A. 2019, MNRAS, 490, 1111, doi: [10.1093/mnras/stz2556](https://doi.org/10.1093/mnras/stz2556)

Ricker, G. R., Winn, J. N., Vanderspek, R., et al. 2014, Society of Photo-Optical Instrumentation Engineers (SPIE) Conference Series, Vol. 9143, Transiting Exoplanet Survey Satellite (TESS), 914320, doi: [10.1117/12.2063489](https://doi.org/10.1117/12.2063489)

Roman, M., & Rauscher, E. 2019, ApJ, 872, 1, doi: [10.3847/1538-4357/aafdb5](https://doi.org/10.3847/1538-4357/aafdb5)

Sandford, E., & Kipping, D. 2019, AJ, 157, 42, doi: [10.3847/1538-3881/aaef565](https://doi.org/10.3847/1538-3881/aaef565)

Seager, S. 2010, Exoplanets

Seager, S., & Sasselov, D. D. 2000, ApJ, 537, 916, doi: [10.1086/309088](https://doi.org/10.1086/309088)

Sheppard, K. B., Welbanks, L., Mandell, A. M., et al. 2021, AJ, 161, 51, doi: [10.3847/1538-3881/abc8f4](https://doi.org/10.3847/1538-3881/abc8f4)

Sing, D. K., Fortney, J. J., Nikolov, N., et al. 2016, Nature, 529, 59, doi: [10.1038/nature16068](https://doi.org/10.1038/nature16068)

Virtanen, P., Gommers, R., Oliphant, T. E., et al. 2020, Nature Methods

von Paris, P., Gratier, P., Bordé, P., Leconte, J., & Selsis, F. 2016, A&A, 589, A52, doi: [10.1051/0004-6361/201527894](https://doi.org/10.1051/0004-6361/201527894)

Wakeford, H. R., Sing, D. K., Stevenson, K. B., et al. 2020, AJ, 159, 204, doi: [10.3847/1538-3881/ab7b78](https://doi.org/10.3847/1538-3881/ab7b78)

Welbanks, L., Madhusudhan, N., Allard, N. F., et al. 2019, ApJL, 887, L20, doi: [10.3847/2041-8213/ab5a89](https://doi.org/10.3847/2041-8213/ab5a89)

Williams, P. K. G., Charbonneau, D., Cooper, C. S., Showman, A. P., & Fortney, J. J. 2006, ApJ, 649, 1020, doi: [10.1086/506468](https://doi.org/10.1086/506468)